

ORBITAL PHASE VARIATIONS OF THE ECCENTRIC GIANT PLANET HAT-P-2B

NIKOLE K. LEWIS^{1,2,3}, HEATHER A. KNUTSON⁴, ADAM P. SHOWMAN¹, NICOLAS B. COWAN⁵, GREGORY LAUGHLIN⁶, ADAM BURROWS⁷, DRAKE DEMING⁸, JUSTIN R. CREPP⁹, KENNETH J. MIGHELL¹⁰, ERIC AGOL¹¹, GÁSPÁR Á. BAKOS⁷, DAVID CHARBONNEAU¹², JEAN-MICHEL DÉSSERT^{4,3}, DEBRA A. FISCHER¹³, JONATHAN J. FORTNEY⁶, JOEL D. HARTMAN⁷, SASHA HINKLEY¹⁴, ANDREW W. HOWARD¹⁵, JOHN ASHER JOHNSON¹⁴, MELODIE KAO⁴, JONATHAN LANGTON¹⁶, GEOFFREY W. MARCY¹⁷, JOSHUA N. WINN¹⁸

Accepted to the Astrophysical Journal

ABSTRACT

We present the first secondary eclipse and phase curve observations for the highly eccentric hot Jupiter HAT-P-2b in the 3.6, 4.5, 5.8, and 8.0 μm bands of the *Spitzer Space Telescope*. The 3.6 and 4.5 μm data sets span an entire orbital period of HAT-P-2b ($P = 5.6334729$ d), making them the longest continuous phase curve observations obtained to date and the first full-orbit observations of a planet with an eccentricity exceeding 0.2. We present an improved non-parametric method for removing the intrapixel sensitivity variations in *Spitzer* data at 3.6 and 4.5 μm that robustly maps position-dependent flux variations. We find that the peak in planetary flux occurs at 4.39 ± 0.28 , 5.84 ± 0.39 , and 4.68 ± 0.37 hours after periapse passage with corresponding maxima in the planet/star flux ratio of $0.1138\% \pm 0.0089\%$, $0.1162\% \pm 0.0080\%$, and $0.1888\% \pm 0.0072\%$ in the 3.6, 4.5, and 8.0 μm bands respectively. Our measured secondary eclipse depths of $0.0996\% \pm 0.0072\%$, $0.1031\% \pm 0.0061\%$, $0.071\%_{-0.013\%}^{+0.029\%}$, and $0.1392\% \pm 0.0095\%$ in the 3.6, 4.5, 5.8, and 8.0 μm bands respectively indicate that the planet cools significantly from its peak temperature before we measure the dayside flux during secondary eclipse. We compare our measured secondary eclipse depths to the predictions from a one-dimensional radiative transfer model, which suggests the possible presence of a transient day side inversion in HAT-P-2b's atmosphere near periapse. We also derive improved estimates for the system parameters, including its mass, radius, and orbital ephemeris. Our simultaneous fit to the transit, secondary eclipse, and radial velocity data allows us to determine the eccentricity ($e = 0.50910 \pm 0.00048$) and argument of periapse ($\omega = 188.09^\circ \pm 0.39^\circ$) of HAT-P-2b's orbit with a greater precision than has been achieved for any other eccentric extrasolar planet. We also find evidence for a long-term linear trend in the radial velocity data. This trend suggests the presence of another substellar companion in the HAT-P-2 system, which could have caused HAT-P-2b to migrate inward to its present-day orbit via the Kozai mechanism.

Subject headings: planets and satellites: general, planets and satellites: individual: HAT-P-2b, techniques: photometric, methods: numerical, atmospheric effects

¹ Department of Planetary Sciences and Lunar and Planetary Laboratory, The University of Arizona, Tucson, AZ 85721, USA

² Department of Earth, Atmospheric and Planetary Sciences, Massachusetts Institute of Technology, Cambridge, MA 02139, USA; nklewis@mit.edu

³ Sagan Postdoctoral Fellow

⁴ Division of Geological and Planetary Sciences, California Institute of Technology, Pasadena, CA 91125, USA

⁵ Center for Interdisciplinary Exploration and Research in Astrophysics and Department of Physics and Astronomy, Northwestern University, 2131 Tech Drive, Evanston, IL 60208, USA

⁶ Department of Astronomy & Astrophysics, University of California, Santa Cruz, CA 95064, USA

⁷ Dept. of Astrophysical Sciences, Princeton University, Princeton, NJ 08544, USA

⁸ Dept. of Astronomy, University of Maryland, College Park, MD, 20742, USA

⁹ Department of Physics, University of Notre Dame, Notre Dame, IN 46556, USA

¹⁰ National Optical Astronomy Observatories, Tucson, AZ 85726, USA

¹¹ Dept. of Astronomy, University of Washington, Seattle, WA 98195, USA

¹² Harvard-Smithsonian Center for Astrophysics, 60 Garden St., Cambridge, MA 02138, USA

¹³ Department of Astronomy, Yale University, New Haven, CT 06511, USA

¹⁴ Department of Astrophysics, California Institute of Technology, MC 249-17, Pasadena, CA 91125, USA

¹⁵ Institute for Astronomy, University of Hawaii, 2680 Woodlawn Drive, Honolulu, HI 96822, USA

¹⁶ Department of Physics, Principia College, 1 Maybeck Place, Elsah, IL 62028, USA

¹⁷ Department of Astronomy, University of California, Berkeley, CA 94720, USA

¹⁸ Department of Physics, and Kavli Institute for Astrophysics and Space Research, Massachusetts Institute of Technology, Cambridge, MA 02139

1. INTRODUCTION

The supermassive ($M_p = 9 M_J$) Jupiter sized ($R_p = 1 R_J$) planet HAT-P-2b (aka HD 147506b) was first discovered from transit observations by Bakos et al. (2007b) using the HATNet (Bakos et al. 2002, 2004) network of ground-based telescopes. Follow-up radial velocity measurements of the HAT-P-2 system revealed that the orbit of HAT-P-2b is highly eccentric ($e = 0.5$ Bakos et al. 2007b; Loeillet et al. 2008). Only a handful of transiting exoplanets have been shown to possess eccentricities in excess of that of Mercury ($e = 0.2$), which has made HAT-P-2b an interesting target for many theoretical studies concerning the evolution of the HAT-P-2 system (Jackson et al. 2008; Fabrycky 2008; Matsumura et al. 2008; Baraffe et al. 2008). Because of its mass, HAT-P-2b represents a class of exoplanets that provides an important link between extrasolar giant planets and low-mass brown dwarfs (Baraffe et al. 2008). Observational constraints on the basic atmospheric properties of HAT-P-2b will provide an important probe into the structure and evolution of not only HAT-P-2b, but an entire class of massive extrasolar planets.

Atmospheric circulation models for planets on eccentric orbits show significant variations in atmospheric temperature and wind speeds that provide an important probe into atmospheric radiative and dynamical timescales (Langton & Laughlin 2008; Lewis et al. 2010; Cowan & Agol 2011; Kataria et al. 2012). The incident flux on HAT-P-2b from its stellar host at periape is ten times that at apoapse, which should cause large variations in atmospheric temperature, wind speeds, and chemistry. Heating and cooling rates for HAT-P-2b can be constrained by measuring planetary brightness as a function of time. Such observations are analogous to previous phase curve observations of HD 189733b using the *Spitzer Space Telescope*, which provided the first clear observational evidence for atmospheric circulation in an exoplanet atmosphere (Knutson et al. 2007, 2009b, 2012).

HAT-P-2b's large orbital eccentricity makes it an ideal target for investigating hot Jupiter migration mechanisms. Gas giant planets such as HAT-P-2b are expected to form beyond the ice line in their protoplanetary disk far from their stellar hosts. HAT-P-2b currently resides at a semi-major axis of 0.07 AU from its host star, indicating that it must have migrated inward via a process such as gas disk migration (Lin et al. 1996), planet-planet scattering (Rasio & Ford 1996), secular interactions (Wu & Lithwick 2011), or Kozai migration (Weidenschilling & Marzari 1996; Naoz et al. 2011). HAT-P-2b's close-in and highly eccentric orbit favors one of the latter three mechanisms since disk migration tends to damp out orbital eccentricities. For Kozai migration, the presence of a third body with at least as much mass as HAT-P-2b is needed. In this study we present six years of radial velocity measurements for this system, which allow us to search for the presence of a massive third body in the HAT-P-2 system.

Here we present our analysis of the 3.6 and 4.5 μm full-orbit phase curves of the HAT-P-2 system, which include two secondary eclipses and one transit at each wavelength. These full-orbit phase curves represent the longest continuous phase observations ever obtained by the *Spitzer Space Telescope*. The orbital period of HAT-

P-2b (5.6334729 d) is more than 2.5 times that of other exoplanets with published full-orbit phase curve observations: WASP-12b (Cowan et al. 2012a) and HD 189733b (Knutson et al. 2012). Additionally, we present an analysis of previous partial orbit phase curve and secondary eclipse *Spitzer* observations at 8.0 and 5.8 μm respectively. We use these observations to characterize the changes in the planet's emission spectrum as a function of orbital phase and to probe the atmospheric chemistry and circulation regime of HAT-P-2b. The following sections describe our observations and data reduction methods (§2) and the results of our analysis (§3). Section 4 discusses the results from our analysis of the *Spitzer* data and compares them to predictions from atmospheric models for HAT-P-2b. Additionally, we discuss trends in our radial velocity data that indicate the presence of an additional body in HAT-P-2 system in Section 4. Section 5 overviews the main conclusions from our analysis and presents ideas for future work.

2. OBSERVATIONS

We analyze nearly 300 hours of observation of HAT-P-2 at 3.6 μm and 4.5 μm obtained during the post-cryogenic mission of the *Spitzer Space Telescope* (Werner et al. 2004) using the IRAC instrument (Fazio et al. 2004) in subarray mode. The observation periods were UT 2010 March 28 to UT 2010 April 03 and UT 2011 July 09 to UT 2011 July 15 for the 3.6 and 4.5 μm bandpasses respectively. Both observations cover a period just over 149 hours with two approximately 2-hour breaks for data downlink, corresponding to ~ 1.2 million images in each bandpass. Each observation begins a few hours before the secondary eclipse of the planet, continues through planetary transit, and ends a few hours after the subsequent planetary secondary eclipse.

We also analyze observations of the HAT-P-2 system at 5.8 μm and 8.0 μm obtained during the cryogenic phase of the *Spitzer Space Telescope* mission. The 5.8 μm observations cover a single secondary eclipse of the planet that occurs on UT 2009 March 16. The 8.0 μm observations cover a portion of the planet's orbit that includes transit, periape passage, and secondary eclipse on UT 2007 September 10-11. The 5.8 μm observations were obtained using subarray mode, while the 8.0 μm observations were obtained using the full IRAC array. We obtain our 3.6, 4.5, 5.8, and 8.0 μm photometry from the Basic Calibrated (BCD) files produced by version 18.18.0 of the *Spitzer* analysis pipeline.

In subarray mode, 32×32 pixel images are stored in sets of 64 as a single FITS file with a single header. We calculate the BJD.UTC at mid-exposure for each image from time stamp stored in the MBJD_OBS keyword of the FITS header, which corresponds to the start of the first image in each set of 64. We assume uniform spacing of the images over the time period defined by the AINTBEG and ATIMMEEND header keywords. The image spacing is roughly equal to the 0.4 s exposure time selected for the 3.6, 4.5, and 5.8 μm observations of HAT-P-2 ($K_{mag} = 7.60$). For the 8.0 μm full array observations, the MBJD_OBS, AINTBEG, and ATIMMEEND header keywords are used to calculate the BJD.UTC at mid-exposure for each image, which are spaced by roughly the 12.0 s exposure time. In order to convert from UTC to TT timing standards as suggested

by Eastman et al. (2010), 66.184 s would be added to our BJD-UTC values. We report all of our timing measurements using BJD-UTC for consistency with other studies.

2.1. 3.6 and 4.5 μm Photometry

We determine the background level in each image from the region outside of a ten pixel radius from the central pixel. This minimizes contributions from the wings of the star’s point spread function while still retaining a substantial statistical sample. We iteratively trim 3σ outliers from the background pixels then fit a Gaussian to a histogram of the remaining pixel values to estimate a sky value. The background flux is 0.6% and 0.2% of the total flux in the science aperture for 3.6 and 4.5 μm observations respectively. We correct for transient hot pixels by flagging pixels more than 4.5σ away from the median flux at a given pixel position across each set of 64 images then replacing flagged pixels by their corresponding position median value.

Several different methods exist to determine the stellar centroid on the *Spitzer* array such as flux-weighted centroiding (e.g. Knutson et al. 2008), Gaussian centroiding, and least asymmetry methods (e.g. Stevenson et al. 2010; Agol et al. 2010). We compare photometry calculated using both Gaussian and flux-weighted centroiding estimates and find that for the HAT-P-2 data flux-weighted centroiding produces the smallest scatter in the final light curve solutions. This is in contrast with the work by Stevenson et al. (2010) and Agol et al. (2010), which advocate Gaussian fits and least asymmetry methods to determine the stellar centroid for observations lasting less than 10 hours. We find that flux-weighted centroids give more stable position estimates over long periods, especially if the stellar centroid crosses a pixel boundary during the duration of the observation. For these data, we calculate the flux-weighted centroid for each background subtracted image using a range of aperture sizes from 2.0 to 5.0 pixels in 0.5 pixel increments. We find that the stellar centroid aperture sizes that best reduce the scatter in the final time series are 4.5 and 3.5 pixels for the 3.6 μm and 4.5 μm observations respectively.

We estimate the stellar flux from each background subtracted image using circular aperture photometry. A range of aperture sizes from 2.0 to 5.0 pixels in 0.25 pixel increments were tested to determine the optimal aperture size for each observation. Additionally, we tested time-varying aperture sizes based on the noise pixel parameter described in the Appendix. We find that we obtain the lowest standard deviation of the residuals from our best-fit solution at 3.6 μm using a variable aperture size given by the square-root of the measured noise pixel value for each image (median aperture size of 2.4 pixels). For the 4.5 μm observations we find that a fixed 2.25 pixel aperture gives the lowest scatter in the final solution. We remove outliers from our final photometric data sets by discarding points more than 4.5σ away from a moving boxcar median 16 points wide. We find that using a narrower median filter or larger value for the outlier cutoff will miss some of the significant outliers. We also find that using a wider median filter or smaller value for the outlier cutoff will often selectively trim the points at the top and bottom of the ‘saw-tooth’ pattern seen in the resulting photometry for the 3.6 and 4.5 μm observa-

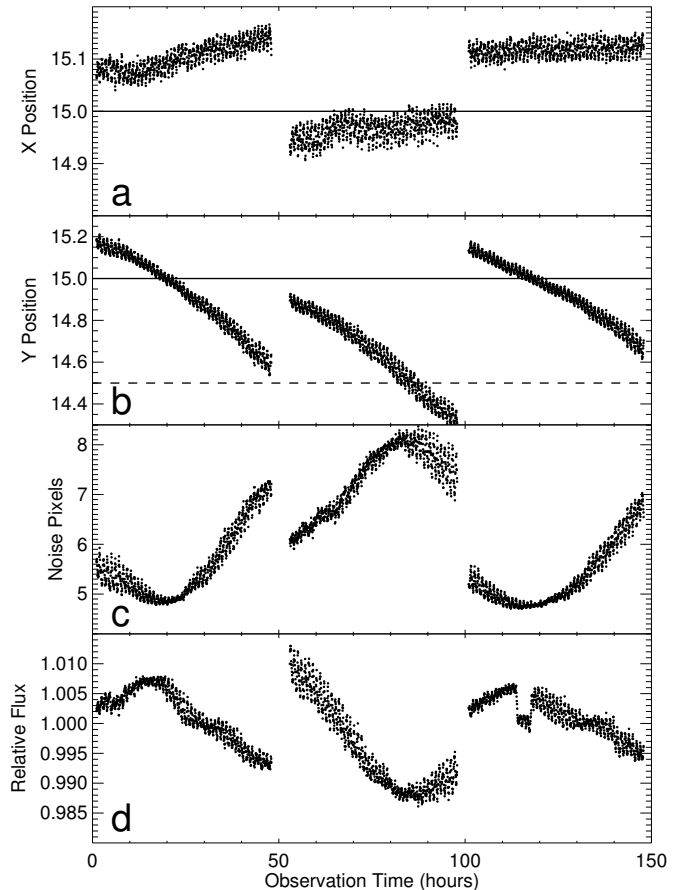


Figure 1. Measured x (a), y (b), noise pixels (c), and raw photometry (d) as a function of time from the start of observation for the 3.6 μm phase curve observations. Data have been binned into three minute intervals. In panels a and b solid horizontal lines indicate the pixel center while dashed horizontal lines indicate a pixel edge. Gaps in the data are due to spacecraft downlinks. Jumps in position, noise pixels, and relative flux after each downlink period are the result of stellar reacquisition. The pointing oscillations and long-term drift in the y direction are due to well-known instrumental effects, and are present in all *Spitzer* observations.

tions (Figures 1 and 2), which is the result of intrapixel sensitivity variations discussed in the Appendix.

2.2. 5.8 μm Photometry

For our 5.8 μm data set, we determine the background level in each image using the same methodology as presented for the 3.6 and 4.5 μm data sets (§2.1). The background flux is 0.6% of the total flux in the science aperture. We tested both flux-weighted and Gaussian fits to the image methods of determining the stellar centroid. For the Gaussian fits to the image we first fit the image allowing both the x and y width of the Gaussian to vary. We then refit the same data set using a symmetric fixed width for the Gaussian that is the mean of the previous x and y widths. We find that Gaussian fits to the image give a lower standard deviation of the residuals in the final fits compared with flux-weighted centroids. This preference for the Gaussian centroiding method is likely the result of the short-time scale of these observations compared with the 3.6 and 4.5 μm observations and the less than 0.1 pixel change in the stellar centroid position over the course of the observation.

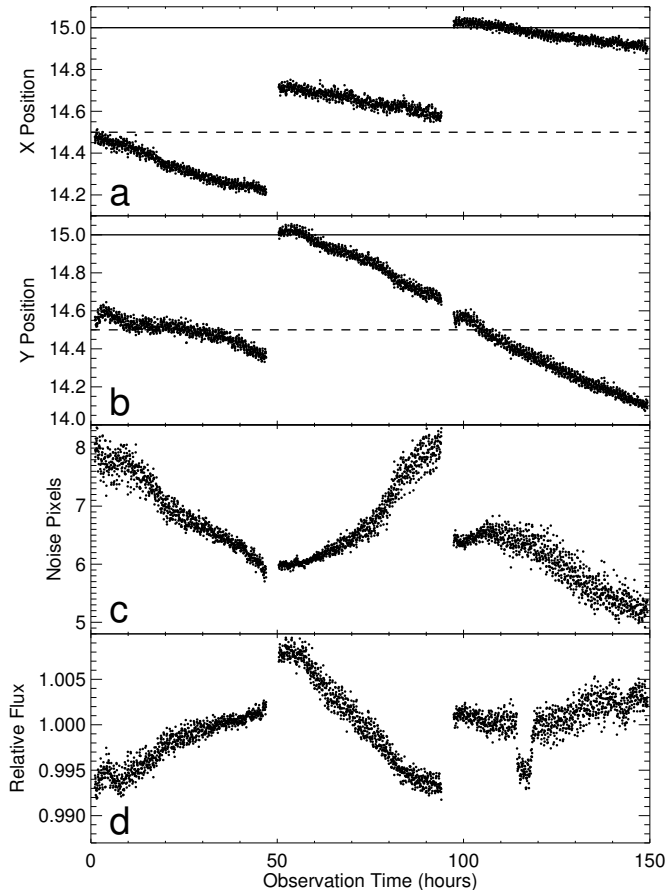


Figure 2. Measured x (a), y (b), noise pixels (c), and raw photometry (d) as a function of time from the start of observation for the $4.5 \mu\text{m}$ phase curve observations. Data have been binned into three minute intervals. In panels a and b solid horizontal lines indicate the pixel center while dashed horizontal lines indicate a pixel edge; see Figure 1 for a complete description.

We estimate the stellar flux from each background subtracted image using circular aperture photometry for a range of apertures sizes from 2.0 to 5.0 pixels in 0.25 pixel increments. We find that an aperture size of 2.5 pixels gives the lowest standard deviation of the residuals in the final fits. We remove outliers in our data set more than 3.0σ away from a moving boxcar median 50 points wide. Figure 3 show our resulting photometry for the $5.8 \mu\text{m}$ observations. We test for possible intrapixel sensitivity variations using the methodology discussed in the Appendix, but find that including intrapixel sensitivity corrections actually degraded the precision of the final solution.

2.3. $8.0 \mu\text{m}$ Photometry

Unlike the 3.6, 4.5, and $5.8 \mu\text{m}$ data, the $8.0 \mu\text{m}$ data were observed in the full-array (256×256 pixels) mode of the IRAC instrument. Our photometry determines the flux from the star in a circular aperture of variable radius, as well as the background thermal emission surrounding the star. We calculate two values of the background, using different spatial regions of the frame. First, we calculate the background that applies to the entire frame. Second, we isolate an annulus between 6 and 35 pixels from the star. In each region (entire frame, or annulus) we calculate the histogram of intensity values from the

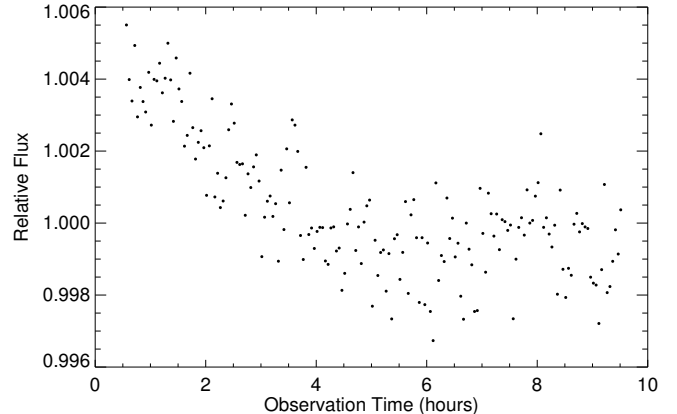


Figure 3. Raw photometry as a function of time from the start of observation for the $5.8 \mu\text{m}$ secondary eclipse observation. Data have been binned into three minute intervals. Note the downward slope in the relative flux values as a function of time.

pixels within the region, and we fit a Gaussian to that histogram. We use the centroid of that Gaussian as the adopted background value. This method has the advantage of being insensitive to ‘hot’ or otherwise discrepant values. We find that using the background values calculated from the region near the star, as opposed to the entire frame, produces a lower scatter in the residuals in our final solution.

We locate the center of the star by fitting a 2-D Gaussian to a 3×3 -pixel median filtered version of the frame; we find that this method produces slightly better photometric precision than using a center-of-light algorithm. We estimate the stellar flux from each background subtracted image using circular aperture photometry for a range of apertures sizes from 2.0 to 5.0 pixels in 0.25 pixel increments. We find that an aperture size of 3.5 pixels gives the lowest standard deviation of the residuals in the final fits. We remove outliers in our data set more than 3.0σ away from a moving boxcar median 50 points wide. Figure 4 show our resulting photometry for the $8.0 \mu\text{m}$ observations. We test for possible intrapixel sensitivity variations using the methodology discussed in the Appendix, but find that including intrapixel sensitivity corrections actually degraded the precision of the final solution.

2.4. Flux Ramp Correction

Our data exhibit a ramp-like increase, or decrease, in the flux values at the start of each observation and after each break in the 3.6 and $4.5 \mu\text{m}$ data for downlink. This ramp in the flux values has been previously noted for IRAC $8.0 \mu\text{m}$ observations (e.g. Knutson et al. (2007, 2009a); Agol et al. (2010)) as well as 3.6 and $4.5 \mu\text{m}$ observations (e.g. Beerer et al. (2011); Todorov et al. (2012)). While the precise nature of this ramp is not well-understood, it can be at least partially attributed to thermal settling of the telescope at a new pointing, which contributes an additional drift in position. However, we see that the ramp often persists beyond this initial drift in position, and we therefore speculate that there is an additional component analogous to the effect observed at long wavelengths due to charge-trapping in the array. We tested several functional forms to describe this ramp,

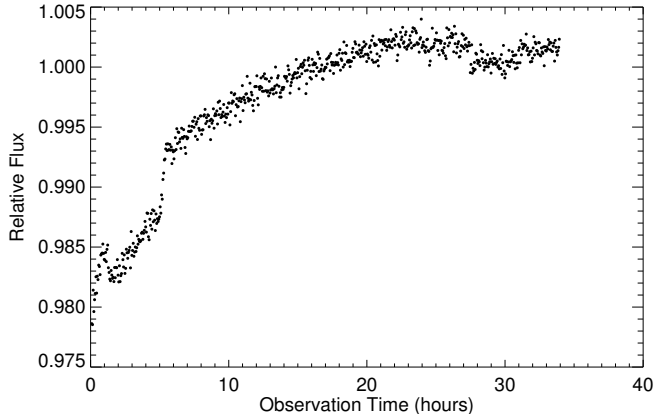


Figure 4. Raw photometry as a function of time from the start of observation for the $8.0 \mu\text{m}$ partial orbit phase curve observation. Data have been binned into three minute intervals. Note the strong exponential growth of the relative flux values as a function of time.

including quadratic, logarithmic, and linear functions of time, but find that functional form that gives us the best correction is given by the formulation presented in Agol et al. (2010):

$$F'/F = 1 \pm a_1 e^{-t/a_2} \pm a_3 e^{-t/a_4} \quad (1)$$

where F' is the measured flux, F is the stellar flux incident on the array, t is the time from the start of the observation in days, and $a_1 - a_4$ are free parameters in the fit.

We find that in the 3.6 and $4.5 \mu\text{m}$ data the asymptotic shape of the ramp converges on timescales less than an hour for most of the data segments. Instead of including parameters in our fits for this ramp behavior, we instead elect to simply trim the first hour at the start of each observation and subsequent downlinks. This reduces the complexity of our fits while avoiding possible correlations between the shape of the underlying phase curve of HAT-P-2b and the ramp function. We find that the ramp persists beyond the one hour mark at the start of the $3.6 \mu\text{m}$ observations, which affects the shape of the first observed secondary eclipse and therefore include a ramp correction for that data segment. For the $5.8 \mu\text{m}$ data, we find that the flux asymptotically decays from the start of the observation (Figure 3). This decrease in the $5.8 \mu\text{m}$ flux is also apparent in the derived background flux values and has been previously noted by studies such as Stevenson et al. (2011). As seen in Figure 4, the $8.0 \mu\text{m}$ data exhibit the well know asymptotic increase in flux (e.g. Knutson et al. 2007, 2009a; Agol et al. 2010).

In order to select the best functional form for the ramp correction in each data set we use the Bayesian Information Criterion (BIC), defined as

$$BIC = \chi^2 + k \ln(n) \quad (2)$$

where k is the degrees of freedom in the fit and n is the total number of points in the fit (Liddle 2007). This allows us to determine if we are ‘over-fitting’ the data by including additional parameters to describe the ramp correction in our fits. We find that for the $3.6 \mu\text{m}$ data set using only a single exponential gives us the lowest BIC value. For the $8.0 \mu\text{m}$ data, using all the terms ($a_1 - a_4$) in Equation 1 with no trimming of the data near the start

of the observation gives us the lowest BIC value. For the $5.8 \mu\text{m}$ data, we find using a single decaying exponential gives the lowest BIC if we trim data within 30 minutes of the start of the observation. Trimming significantly more or less than this amount either gives a higher BIC or reduces the amount of out of eclipse data to less than the eclipse duration.

2.5. Transit and Eclipse Fits

We model our transit and eclipse events using the equations of Mandel & Agol (2002) modified to account for the orbital eccentricity, e , and argument of periape, ω , of the HAT-P-2 system. For an eccentric system the normalized separation of the planet and star centers, z , is given by

$$z = \frac{r(t)}{R_\star} \sqrt{1 - (\sin i * \sin(\omega + f(t)))^2} \quad (3)$$

where $r(t)$ is the radial planet-star distance as a function of time, R_\star is the stellar radius, i is the orbital inclination of the planet, and $f(t)$ is the true anomaly as a function of time. The $r(t)/R_\star$ term in Equation 3 is calculated as

$$\frac{r(t)}{R_\star} = \frac{a}{R_\star} \frac{1 - e^2}{1 + e \cos(f(t))}. \quad (4)$$

The true anomaly angle (f) that appears in both Equations 3 and 4 is determined using Kepler’s equation (Murray & Dermott 1999) and is a function of e , ω , and the orbital period of the planet, P . Because of the degeneracies that exist between e , ω and P in determining $f(t)$ we elect to not use P as a free parameter in our fits. Instead we fix P to the value reported in Pál et al. (2010), 5.6334729 d. We further minimize correlations in our solutions for e and ω by solving for the Lagrangian orbital elements $k \equiv e \cos \omega$ and $h \equiv e \sin \omega$.

In addition to the parameters that define the orbit of HAT-P-2b, we solve for the fractional planetary radius, R_p/R_\star . Because $R_p/R_\star < 0.1$ for HAT-P-2b (Pál et al. 2010; Bakos et al. 2007b), there exists a strong correlation between i and a/R_\star in the transit solution (Winn et al. 2007b; Pál 2008). We instead solve for the parameters b^2 and ζ/R_\star as suggested by Bakos et al. (2007a) and Pál et al. (2010) where

$$b = \frac{a}{R_\star} \frac{1 - e^2}{1 + h} \cos i \quad (5)$$

and

$$\frac{\zeta}{R_\star} = \frac{a}{R_\star} \frac{2\pi}{P} \frac{1}{\sqrt{1 - b^2}} \frac{1 + h}{\sqrt{1 - e^2}}. \quad (6)$$

For the transit portion of the light curves we use four parameter nonlinear limb-darkening coefficients for each bandpass calculated by Sing (2010), where we assume a stellar atmosphere with $T_{eff} = 6290$ K, $\log(g) = 4.138$, and $[\text{Fe}/\text{H}] = +0.14$ (Pál et al. 2010). For the secondary eclipse portion of the light curves we treat the planet as a uniform disk and scale the ingress and egress to match the amplitude of the phase curve (§2.6), which varies significantly over the duration of the eclipse and is therefore poorly approximated by a constant value. The secondary eclipse depth is defined by the average of the ingress and egress amplitudes.

For the 3.6 and 4.5 μm datasets, we use nine free parameters to constrain the properties of the planetary orbit, transit, and secondary eclipse. The 8.0 μm observations only include one secondary eclipse and therefore only require eight free parameters to constrain the same system properties. The 5.6 μm data set includes only the secondary eclipse portion of the light curve. We therefore elect to only allow the secondary eclipse depth and timing to vary for the 5.6 μm data and fix a/R_\star , i , e , ω , and R_p/R_\star to the average values from the 3.6, 4.5, and 8.0 μm data sets.

2.6. Phase Curve Fits

The functional form of the phase curve for a planet on an eccentric orbit is not well defined. Unlike close-in, tidally locked planets on circular orbits, eccentric planets experience time-variable heating and non-synchronous rotation rates. Previous studies by Langton & Laughlin (2008) and Cowan & Agol (2011) have investigated theoretical light curves for planets on eccentric orbits using two-dimensional hydrodynamic simulations and semi-analytic model atmospheres respectively. We also developed a three-dimensional atmospheric model for HAT-P-2b that couples radiative and dynamical processes to further investigate possible phase curve functional forms that will be presented in a future paper. The functional forms for the phase curves described here all provide a reasonable fit to the theoretical light curves presented in Langton & Laughlin (2008), Cowan & Agol (2011), and from our three-dimensional atmospheric model.

To first order, the flux from the planet is proportional to the inverse square of the distance between the planet and host star, $r(t)$. This assumes that the planet has a constant albedo and responds instantaneously and uniformly to changes in the incident stellar flux. We know that there must exist a lag in the peak of the incident stellar flux and the peak of the planet's temperature since atmospheric radiative timescales are finite (Langton & Laughlin 2008; Iro & Deming 2010; Lewis et al. 2010; Cowan & Agol 2011). Our first functional form for the phase variation of HAT-P-2b is a simple $1/r(t)^2$ with a phase lag:

$$F(f) = F_0 + c_1(1 + \cos(f - c_2))^2 \quad (7)$$

where f is the true anomaly and $c_1 - c_2$ are free parameters in the fit. The $1 + \cos(f - c_2)$ is a simplified form of the denominator of Equation 4 for $r(t)$. We also test a simpler form of Equation 7 given by

$$F(f) = F_0 + c_1 \cos(f - c_2) \quad (8)$$

where $c_1 - c_2$ are free parameters in the fit. This functional form of the phase curve is similar to a simple sine or cosine of the orbital phase angle, λ or ξ , used in the case of a circular orbit.

We also find that a Lorentzian function of time provides a reasonable representation of the expected shape of the orbital phase curve for HAT-P-2b. This is not surprising given that we expect the flux from the planet to vary as $1/r(t)^2$ with a time lag between the minimum of the planetary distance and the peak of the planetary flux. We test both symmetric and asymmetric Lorentzian functions of the time from periapse passage,

t , given by

$$F(t) = F_0 + \frac{c_1}{u(t)^2 + 1} \quad (9)$$

where

$$u(t) = (t - c_2)/c_3 \quad (10)$$

in the symmetric case and

$$u(t) = \begin{cases} (t - c_2)/c_3 & \text{if } t < c_2; \\ (t - c_2)/c_4 & \text{if } t > c_2 \end{cases} \quad (11)$$

in the asymmetric case. In Equations 9, 10, and 11 $c_1 - c_4$ are free parameters in the fit. The Lorentzian functional form for the phase curve is especially useful since the c_2 parameter gives the offset between the time of periapse passage and the peak of the planet's flux and the $c_3 - c_4$ parameters gives an estimate of relevant atmospheric timescales.

We also find that the preferred functional form for the phase curve of planets on circular orbits described in Cowan & Agol (2008) provides a reasonable fit to our theoretical light curves if the orbital phase angle, ξ , is replaced by the true anomaly, f . In this case

$$F(\theta) = F_0 + c_1 \cos(\theta) + c_2 \sin(\theta) + c_3 \cos(2\theta) + c_4 \sin(2\theta) \quad (12)$$

where $c_1 - c_4$ are free parameters in the fit and $\theta = f + \omega + \pi$ such that transit occurs at $\theta = -\pi/2$ and secondary eclipse occurs at $\theta = \pi/2$.

In addition to the functional forms for the phase curve presented above, we also test a flat phase curve, $F(t) = F_0$, to make sure that we are not over-fitting the data with the phase curve parameters. In all cases we tie the F_0 parameter to the secondary eclipse depth to give the appropriate average value of the phase curve during secondary eclipse. We also set any portion of the phase curve that falls below the secondary eclipse depth to zero. During secondary eclipse we no longer see flux from the planet, only the star, therefore the combined star and planetary flux should always be greater than or equal to the flux at the bottom of the secondary eclipse.

We choose the optimal phase curve solution to be the one that gives the lowest BIC value (Equation 2) using a Levenberg-Marguardt non-linear least squares fit to the data (Markwardt 2009). For the 3.6 and 4.5 μm data sets, we also compare the BIC values from each of the three data segments separated by the downlink periods to make sure that the solution is robust at all orbital phases. For the 3.6, 4.5, and 8.0 μm data sets, we find that all of the functional forms presented Section 2.6 provide a significant improvement in the BIC values over the 'flat' phase curve BIC values ($\text{BIC}_{3.6 \mu\text{m}}=1,282,575$; $\text{BIC}_{4.5 \mu\text{m}}=1,459,141$; $\text{BIC}_{8.0 \mu\text{m}}=11,183$). For the 3.6 μm data we obtain the lowest BIC value with a functional form for the phase curve defined by either Equation 8 or Equation 12 with $c_3 - c_4$ fixed at zero ($\text{BIC}=1,278,521$). This is not surprising since basic trigonometric identities make Equation 12 equivalent to Equation 8 if $c_3 - c_4$ can be assumed to be zero. For the 4.5 μm data we obtain the lowest BIC value with a functional form for the phase curve given by Equation 12 with the c_1 and c_3 terms fixed at zero ($\text{BIC}=1,458,842$).

The phase curve model given by Equation 12 also gives us a reasonable improvement in the BIC for our 8.0 μm data set. However, we find that the second harmonic in Equation 12 is highly degenerate with our ramp correction at 8.0 μm such that we cannot reliably constrain the significance of this harmonic in the fit. We instead use the phase curve functional form given by Equation 7, which gives us the lowest BIC for the 8.0 μm data set (BIC=10,945). For the 5.8 μm data, which only span ten hours, we find no statistical difference between solutions with and without parameterizations for planetary phase variations.

2.7. Stellar Variability

HAT-P-2 is a rapidly rotating F star ($v \sin i = 20.7 \text{ km s}^{-1}$). Measurements of the Ca II H & K lines of HAT-P-2 by Knutson et al. (2010) do not detect any significant emission in the line cores, which would suggest a chromospherically quiet stellar host for HAT-P-2b. However, this indicator provides relatively weak constraints on chromospheric activity for F stars, which have strong continuum emission in the wavelengths of the Ca II H & K lines. Ground-based monitoring of HAT-P-2 in the Strömgren b and y bands over a period of more than a year indicates that it varies by less than 0.13% at visible wavelengths. We would expect the star to vary by substantially less than this amount in the infrared, where the flux contrast of spots and other effects is correspondingly reduced. These observations rule out both periodic variability that could be associated with the rotation rate of HAT-P-2 or longer-term trends (G. Henry 2010, private communication). Previous observations find the rotation rate of the star to be on the order of 3.8 d (Winn et al. 2007a) based on the line-of-sight stellar rotation velocity ($v \sin i_*$) and assuming $\sin i_* = 1$, which is roughly 0.6 times the orbital period of HAT-P-2b. We do not expect stellar variability to be significant on the timescales of our observations, but for the sake of completeness we also check this assumption directly using our *Spitzer* data.

We employ two models for stellar variability. The first model is a simple linear function of time given by

$$F_0(t) = d_1 t \quad (13)$$

where t is measured from the predicted center of transit in each observation and d_1 is a free parameter in the fit. The second model we test has the form

$$F_0(t) = d_1 \sin((2\pi/d_2)t - d_3) \quad (14)$$

where t is measured from the predicted center of transit in each observation and $d_1 - d_3$ are free parameters in the fit. Equation 14 attempts to capture stellar variability that is associated with star spots that rotate in and out of view with the d_2 parameter representing the rotation rate of the star.

We find that the linear model for stellar variability does not improve the χ^2 of the fits significantly and in fact increases the BIC (Equation 2). Inclusion of the stellar model given by Equation 14 does improve both the χ^2 and BIC in our fits. However, we find that the solutions for the ‘sine-curve’ model for stellar variability are often degenerate with our models for the phase curve and the

residual ramp at the start of the 3.6 μm observations. We also find that the stellar rotation rate predicted by the d_2 term in Equation 14 differs significantly between the 3.6 and 4.5 μm observations with a rotation rate of 4.3 d preferred for the 3.6 μm data and 3.9 d preferred for the 4.5 μm data. Although these predicted rotation periods are near to the expected 3.8 d rotation period of HAT-P-2, the amplitude of the predicted stellar variations in the mid-infrared seem spurious. The amplitude of the predicted stellar flux variations at 3.6 and 4.5 μm are on the order of $\sim 0.1\%$, which is comparable to our upper limit on stellar variability at visible wavelengths (0.13%). We would expect star spots to display much larger variations in the visible than at mid-infrared wavelengths. The amplitude of these stellar variations are also similar to the amplitude of our predicted phase variations. We therefore conclude that our best-fit solutions for the stellar variability are physically implausible, and likely the result from a degeneracy with the other terms in our fits. As we have no convincing evidence for stellar variability, we assume that the star’s flux is constant in our final fits.

2.8. Radial Velocity Measurements

Since the discovery of HAT-P-2b by Bakos et al. (2007b), the California Planet Search (CPS) team has continued to obtain regular radial velocity (RV) measurements of this system using the HIRES instrument (Vogt et al. 1994) on Keck. We used the CPS pipeline (see, e.g. ?) to measure precise RVs from the high-resolution spectra of HAT-P-2 using a superposed molecular iodine spectrum as a Doppler reference and point spread function calibrant. Previous studies of this system (Bakos et al. 2007b; Winn et al. 2007a; Pál et al. 2010) have included HIRES radial velocity measurements through May 2008 (BJD = 2454603.932112). Here we present 16 additional RV measurements from the HIRES instrument on Keck for a total of 71 data points spanning 6 years (Table 1). We exclude measurements obtained during transit (Winn et al. 2007a) from our fits in order to avoid measurements affected by the Rossiter-McLaughlin effect.

We simultaneously fit for the RV semi-amplitude (K), zero-point (γ), and long term velocity drift ($\dot{\gamma}$) along with the orbital, transit, eclipse, and phase parameters in the 3.6, 4.5, and 8.0 μm data sets separately. We also test for possible curvature in the RV signal ($\ddot{\gamma}$), but find that our derived values for $\ddot{\gamma}$ were consistent with zero. As discussed in Winn (2010), the transit to secondary eclipse timing strongly constrains the $e \cos \omega$ term in our fits, but the $e \sin \omega$ term is better constrained by the inclusion of these RV data. Rapidly rotating stars are known to have an increased scatter in their RV velocity distribution beyond the reported internal errors (as discussed in Bakos et al. 2007b; Winn et al. 2007a). We therefore estimate a stellar jitter term (σ_{jitter}) as described in Section 3.

3. RESULTS

We perform a simultaneous fit and calculate uncertainties for the relevant transit, secondary eclipse, phase curve, radial velocity, flux ramp, and intrapixel sensitivity correction parameters in our data sets using a Markov Chain Monte Carlo (MCMC) method (Ford 2005). For the 3.6, 4.5, and 8.0 μm data sets fit parameters include

Table 1
Radial Velocities for HAT-P-2b from Keck

BJD - 2400000 (days)	RV (m s ⁻¹)	Uncertainty (m s ⁻¹)
53981.777500	-19.17	7.46
53982.871700	-310.87	7.64
53983.814865	538.73	7.81
53984.894980	855.62	7.94
54023.691519	698.64	7.94
54186.998252	696.78	7.72
54187.104158	684.36	6.84
54187.159878	717.17	6.59
54188.016885	757.70	7.00
54188.159622	774.61	6.80
54189.010378	651.86	6.59
54189.088911	635.16	6.48
54189.157721	619.70	7.22
54216.959395	722.59	8.04
54257.756431	27.91	5.79
54257.758677	35.49	6.17
54257.760702	24.33	6.18
54257.794116	-11.70	5.48
54257.796779	-19.01	5.02
54257.799452	-20.94	5.10
54257.802148	-23.48	4.74
54257.804926	-21.89	5.15
54257.807634	-35.65	4.91
54257.810342	-24.40	5.08
54257.813143	-40.82	5.22
54257.815817	-37.08	5.45
54257.818490	-23.98	5.21
54258.024146	-313.00	4.87
54258.027167	-310.40	4.89
54258.030292	-311.56	4.37
54258.033278	-326.04	4.58
54258.042630	-314.19	5.10
54258.045488	-336.27	4.92
54258.048393	-342.10	5.07
54258.051483	-351.92	4.88
54258.054828	-356.80	4.94
54258.058161	-356.72	4.65
54258.061472	-360.49	4.85
54258.064666	-374.47	4.73
54258.099110	-432.29	5.27
54258.102836	-433.53	4.97
54258.106679	-446.91	4.74
54279.876893	371.51	8.26
54285.823854	137.15	5.91
54294.878702	728.72	6.61
54304.864982	588.92	6.07
54305.870122	737.55	6.23
54306.865216	731.39	7.95
54307.912379	456.62	6.39
54335.812619	549.60	6.64
54546.098175	-684.07	7.79
54547.115700	536.15	7.19
54549.050468	754.51	7.26
54602.916550	271.30	6.47
54603.932112	662.48	5.74
54839.166895	-369.59	8.09
55015.871081	679.68	8.89
55350.945695	-513.11	8.45
55465.742817	606.08	6.99
55703.872995	623.50	7.70
55704.836273	377.02	8.02
55705.853346	-535.77	8.12
55706.831645	-257.19	7.57
55707.844353	504.50	7.68
55808.759715	323.97	8.49
55850.695496	557.65	7.37
55932.161110	-241.35	9.48
55945.128011	595.28	8.57
55992.018498	401.30	10.08
56147.753065	553.56	7.95
56149.738596	381.71	8.37

b^2 , ζ/R_* , $e \cos \omega$, $e \sin \omega$, R_p/R_* , transit time, the secondary eclipse depth(s), the phase function coefficients $c_1 - c_4$, a photometric noise term (σ_{phot}), and RV parameters K , γ , $\dot{\gamma}$, σ_{jitter} . For the 3.6 and 8.0 μm data sets we additionally fit for the ramp correction coefficients $a_1 - a_4$. The free parameters in the fit to the 5.8 μm data set are the eclipse time, eclipse depth, ramp correction coefficients $a_1 - a_4$, and σ_{phot} . The value of the stellar flux, F_0 , is inherently accounted for with our intrapixel sensitivity correction method described in the Appendix. Because we do not apply intrapixel sensitivity corrections to our 5.8 and 8.0 μm data sets we additionally fit for F_0 in those cases.

The only parameter held fixed in our analysis is the orbital period (P), the value for which we take from Pál et al. (2010). All other orbital, planetary, phase, and ramp parameters are allowed to vary freely. Initial attempts at fitting just the 3.6 and 4.5 μm transits simultaneously produce a value for P within 1σ of the Pál et al. (2010) value, and we are therefore confident that adopting the Pál et al. (2010) value for P has not introduced any significant errors into our analysis.

We initially attempted to fit for the wavelength independent parameters b^2 , ζ/R_* , $e \cos \omega$, $e \sin \omega$, and T_c simultaneously for the RV, 3.6, 4.5, and 8.0 μm data sets. However, given the size of our data sets (over 2.5 million data points) and the time required to create our ‘pixel-maps’ for the 3.6 and 4.5 μm data (see Appendix), we found it computationally infeasible. It is possible that further improvements to our analysis code, including parallelization, could make the problem more computationally tractable. Such improvements are left for future iterations of our analysis methods.

We plot the normalized time series for the 3.6, 4.5, and 8.0 μm data sets after the best-fit intrapixel sensitivity variations and ramp corrections have been removed in Figure 5. The regions near secondary eclipse and transit for each best fit solution are presented in Figures 6, 7, 8, and 9 for the 3.6, 4.5, 5.8, and 8.0 μm data sets respectively. We also present our best fit solution to the RV data in Figure 10.

We use a total of five independent chains with 10^5 steps per chain in our MCMC analysis. Each chain is initialized at a position in parameter space determined by randomly perturbing the best-fit parameters from a Levenberg-Marquardt non-linear least squares fit to the data (Markwardt 2009). Instead of using a standard χ^2 minimization scheme, we instead opt to maximize the log of the likelihood (L) given by

$$\log(L) = \sum (-\log(2\pi\sigma^2) - (\text{data} - \text{model})^2/(2\sigma^2)), \quad (15)$$

where σ is the relevant error term. This allows us to simultaneously solve for the noise terms σ_{phot} and σ_{jitter} with our other fit parameters (see Carter & Winn 2009, for further discussion of the maximum likelihood method as applied to exoplanet transit observations). After each chain has reached 10^5 steps, we find the the point where $\log(L)$ first surpasses the median $\log(L)$ value and discard all steps up to that point. We then combine the results from our independent chains and find the range about a median value that contains 68% of the values for a given parameter. We set our best-fit parameters equal

Table 2
Global Fit Parameters

Parameter	3.6 μm	4.5 μm	5.8 μm	8.0 μm
<i>Transit Parameters</i>				
R_p/R_\star	0.06821 \pm 0.00075	0.07041 \pm 0.00060	0.06933 ^d	0.0668 \pm 0.0016
b^2	0.122 ^{+0.066} _{-0.078}	0.345 \pm 0.042	...	0.238 ^{+0.096} _{-0.131}
i ($^\circ$)	87.37 ^{+1.34} _{-0.81}	84.91 \pm 0.47	85.97 ^d	86.0 ^{+1.5} _{-1.0}
a/R_\star	9.53 \pm 0.35	8.28 \pm 0.24	8.70 ^d	8.83 ^{+0.67} _{-0.53}
T_c (BJD-2400000) ^a	55288.84988 \pm 0.00060	55756.42520 \pm 0.00067	...	54353.6911 \pm 0.0012
ζ/R_\star (d^{-1})	12.221 \pm 0.058	12.286 \pm 0.057	...	12.21 \pm 0.11
T_{14} (d) ^b	0.1770 \pm 0.0011	0.1813 \pm 0.0013	...	0.1789 \pm 0.0023
T_{12} (d) ^b	0.0128 \pm 0.0010	0.0177 \pm 0.0012	...	0.0144 \pm 0.0021
<i>Secondary Eclipse Parameters</i>				
ϕ_{sec}	0.19177 \pm 0.00029	0.19310 \pm 0.00025	...	0.19253 \pm 0.00048
T_{14} (d) ^b	0.1550 \pm 0.0027	0.1651 \pm 0.0023	...	0.1610 \pm 0.0043
T_{12} (d) ^b	0.01090 \pm 0.00075	0.01444 \pm 0.00083	...	0.0121 \pm 0.0016
1 st Eclipse Depth	0.080% \pm 0.012%	0.1009% \pm 0.0084%
T_c (BJD-2400000) ^a	55284.2967 \pm 0.0014	55751.8795 \pm 0.0011
2 nd Eclipse Depth	0.0993% \pm 0.0090%	0.1057% \pm 0.0090%	0.071% ^{+0.029%} _{-0.013%}	0.1392% \pm 0.0095%
T_c (BJD-2400000) ^a	55289.9302 \pm 0.0014	55757.5130 \pm 0.0011	54906.8561 ^{+0.0076} _{-0.0062}	54354.7757 \pm 0.0022
<i>Orbital & RV Parameters</i>				
$e \cos \omega$	-0.50539 \pm 0.00057	-0.50301 \pm 0.00051	...	-0.50419 \pm 0.00088
$e \sin \omega$	-0.0741 \pm 0.0072	-0.0729 \pm 0.0054	...	-0.0685 \pm 0.0059
e	0.51081 \pm 0.00092	0.50829 \pm 0.00068	0.50910 ^d	0.50885 \pm 0.00097
ω ($^\circ$)	188.34 \pm 0.80	188.25 \pm 0.62	188.09 ^d	187.74 \pm 0.66
T_p (BJD-2400000)	55289.4734 \pm 0.0079	55757.05194 \pm 0.0061	...	54354.3109 \pm 0.0065
K (m s^{-1})	927.0 \pm 5.9	923.0 \pm 5.8	...	923.1 \pm 6.0
γ (m s^{-1})	247.4 \pm 3.7	248.0 \pm 3.6	...	248.0 \pm 3.6
$\dot{\gamma}$ ($\text{m s}^{-1} \text{d}^{-1}$)	-0.0890 \pm 0.0050	-0.0881 \pm 0.0049	...	-0.0886 \pm 0.0058
<i>Phase Curve Parameters</i>				
Functional Form	Eq. (12)	Eq. (12)	Flat	Eq. (7)
c_1	0.0379% \pm 0.0015%	0 (fixed)	...	0.0555% \pm 0.0032
c_2	0.0422% \pm 0.0025%	0.0293% \pm 0.0042%	...	41.8 $^\circ$ \pm 2.7 $^\circ$
c_3	0 (fixed)	0 (fixed)
c_4	0 (fixed)	0.0163% \pm 0.0035%
Amplitude	0.114% \pm 0.010%	0.079% \pm 0.013%
Minimum Flux	0.00014% ^{+0.00927%} _{-0.00014%}	0.0372% ^{+0.0086%} _{-0.0096%}
Minimum Flux Offset (h) ^c	-18.36 ^{+0.18} _{-1.00}	6.71 \pm 0.43
Maximum Flux	0.1139% \pm 0.0089%	0.1162% ^{+0.0089%} _{-0.0071%}	...	0.1888% \pm 0.0072%
Maximum Flux Offset (h) ^c	4.39 \pm 0.28	5.84 \pm 0.39	...	4.68 \pm 0.37
<i>Ramp Parameters</i>				
Functional Form	Eq. (1)	None	Eq. (1)	Eq. (1)
a_1	-0.00134 ^{+0.00105} _{-0.00054}	...	+0.00683 ^{+0.00086} _{-0.00054}	-0.00537 ^{+0.00088} _{-0.00069}
a_2	0.078 ^{+0.050} _{-0.029}	...	0.095 \pm 0.015	0.0195 ^{+0.0067} _{-0.0051}
a_3	0 (fixed)	-0.01765 ^{+0.00053} _{-0.00075}
a_4	0 (fixed)	0.2812 ^{+0.0155} _{-0.0091}
<i>Noise Parameters</i>				
σ_{phot}	0.0042209 \pm 0.0000024	0.0057064 \pm 0.0000032	0.015380 \pm 0.0000034	0.002164 \pm 0.000015
σ_{jitter} (m s^{-1})	26.0 \pm 2.1	25.7 \pm 2.2	...	25.5 \pm 2.1

^a We list all time in BJD_UTC for consistency with other studies; to convert to BJD_TT add 66.184 s.

^b T_{14} is the total transit or eclipse duration. T_{12} is the ingress duration, which equivalent to the egress duration (T_{34}) to within error.

^c Minimum flux offset is measured relative to the center of transit time (T_c). Maximum flux offset is measured relative to the time of periape passage (T_p).

^d Represents average value from 3.6 μm , 4.5 μm and 8 μm analyses. Value held fixed in 5.8 μm analysis.

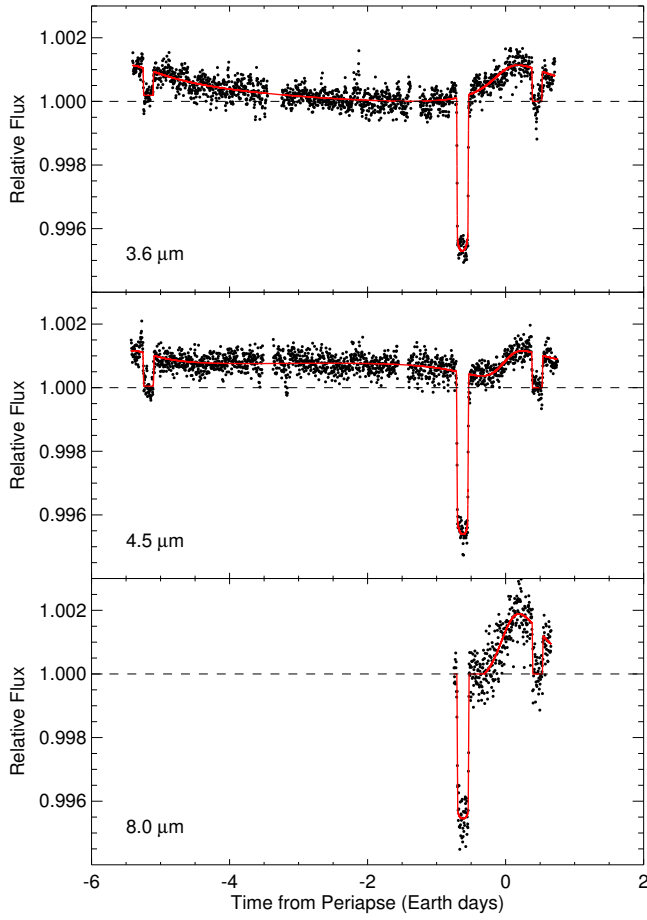


Figure 5. Final 3.6 (top), 4.5 μm (middle), and 8.0 μm photometry (filled circles) after correcting for intrapixel sensitivity variations (3.6 and 4.5 μm) and the ramp-like behavior of the flux with time (3.6 and 8.0 μm), binned into five minute intervals. The best-fit phase, transit and secondary eclipse curves are overlotted as a red line. The dashed line represents the stellar flux level.

to this median value and use this distribution to initially determine the 1σ uncertainties in each of our parameters. For most parameters our error distribution was close to being symmetric about the median value. In the cases where the distribution was significantly asymmetric, we have noted both the positive and negative uncertainties in the parameter value.

We find that there is (‘red’) correlated noise in our data even after the best fit intrapixel sensitivity variations have been removed. To account for correlated noise in our data we first employed the wavelet-based MCMC method described in Carter & Winn (2009). However, we found that our correlated noise could not be treated as a stationary noise parameter. Often we found that fits to the transit and secondary eclipse portions of our phase curves were degraded to introduce ‘red’ noise consistent with other portions of the light curve. As a result, we instead opt to use the ‘residual-permutation’ or ‘prayer-bead’ method to estimate the errors in our parameters in the presence of correlated noise (see, for example Jenkins et al. 2002; Southworth 2008; Bean et al. 2008; Winn

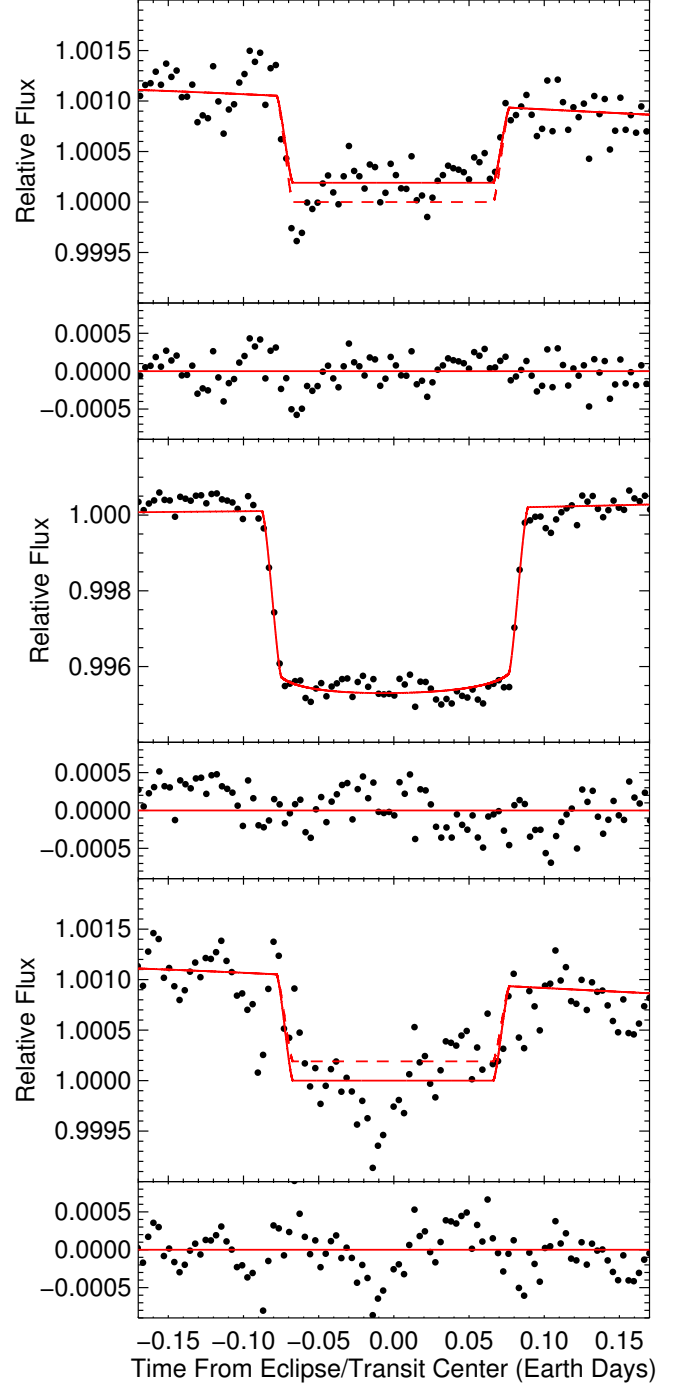


Figure 6. Best-fit transit (middle panel) and secondary eclipse (top and bottom panels) light curves (red lines) for the 3.6 μm observations (black filled circles). The data have been binned by five minute intervals. Residuals for each of the fits are presented just below each transit or secondary eclipse event. The dashed red lines in the secondary eclipse panels show the best fit light curve corresponding to the other secondary eclipse.

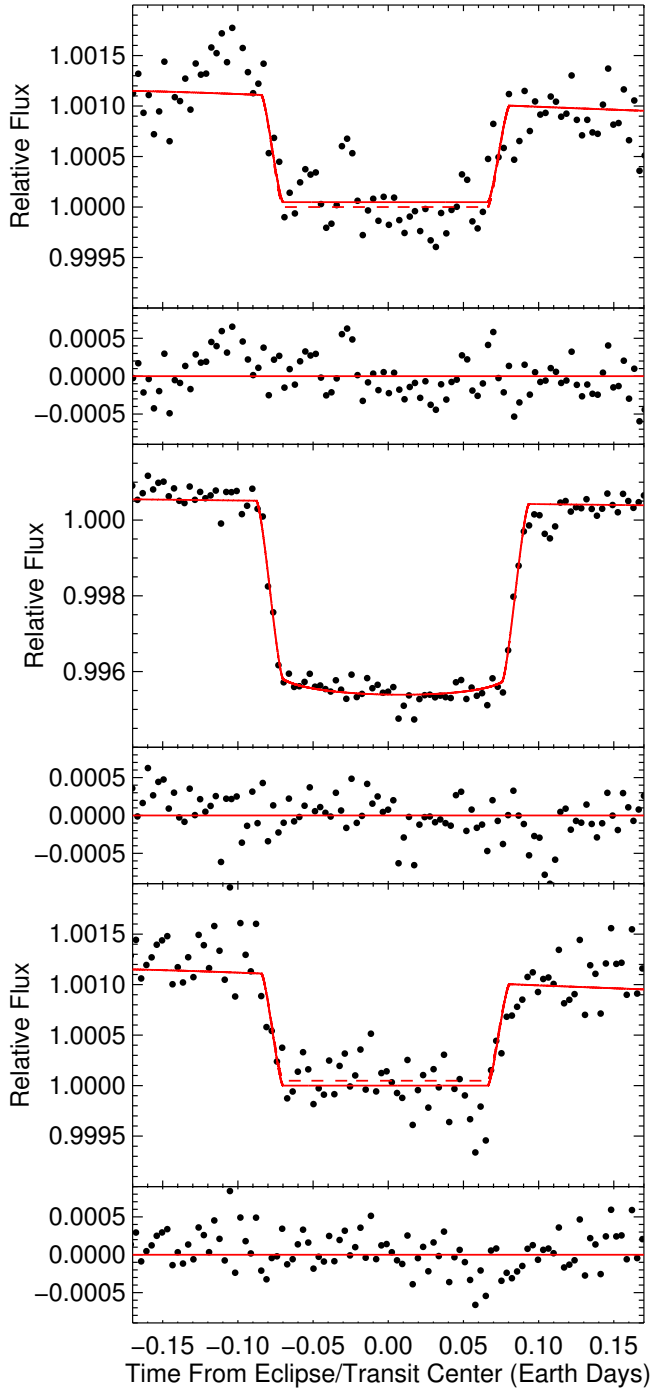


Figure 7. Best-fit transit (middle panel) and secondary eclipse (top and bottom panels) light curves (red lines) for the $4.5 \mu\text{m}$ observations (black filled circles). The data have been binned by five minute intervals. Residuals for each of the fits are presented just below each transit or secondary eclipse event. The dashed red lines in the secondary eclipse panels show the best fit light curve corresponding to the other secondary eclipse.

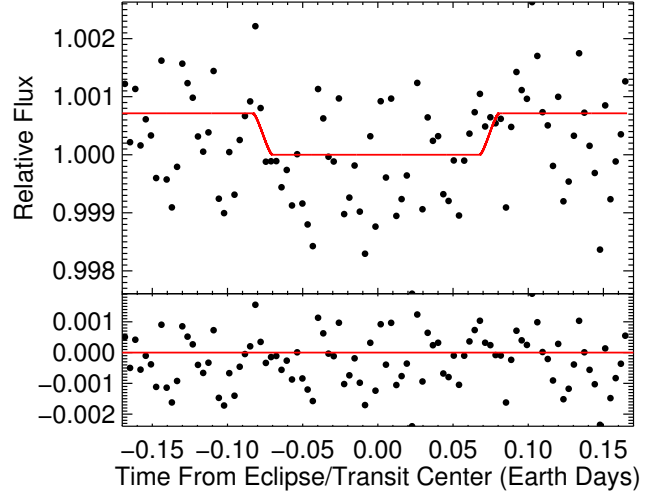


Figure 8. Best-fit secondary eclipse light curve (red line) for the $5.8 \mu\text{m}$ observations (black filled circles). The data have been binned by five minute intervals. Residuals to the fit are presented just below the secondary eclipse event.

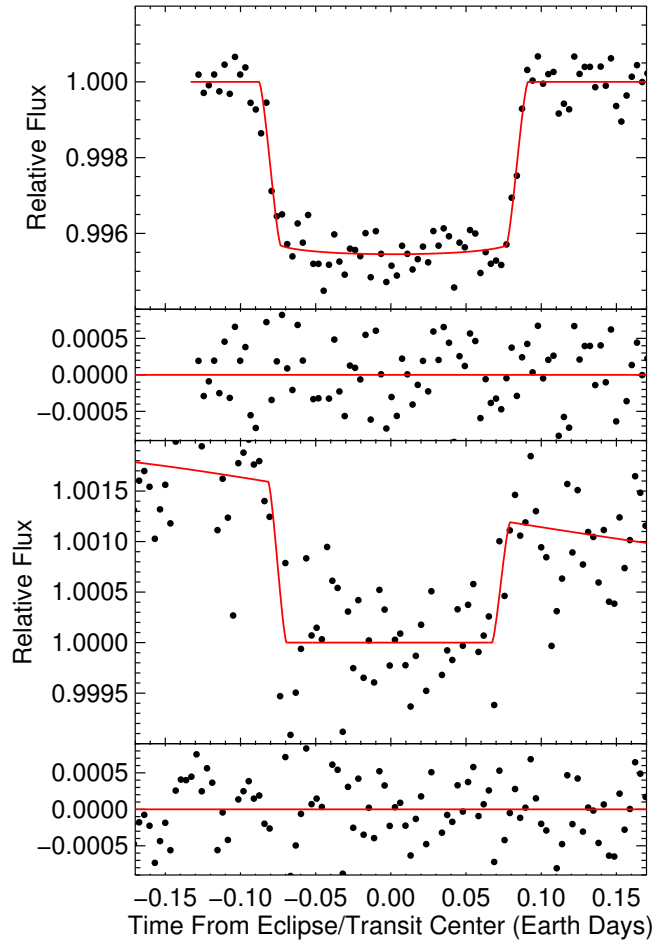


Figure 9. Best-fit transit (top panel) and secondary eclipse (bottom panel) light curves (red lines) for the $8.0 \mu\text{m}$ observations (black filled circles). The data have been binned by five minute intervals. Residuals for each of the fits are presented just below each transit or secondary eclipse event.

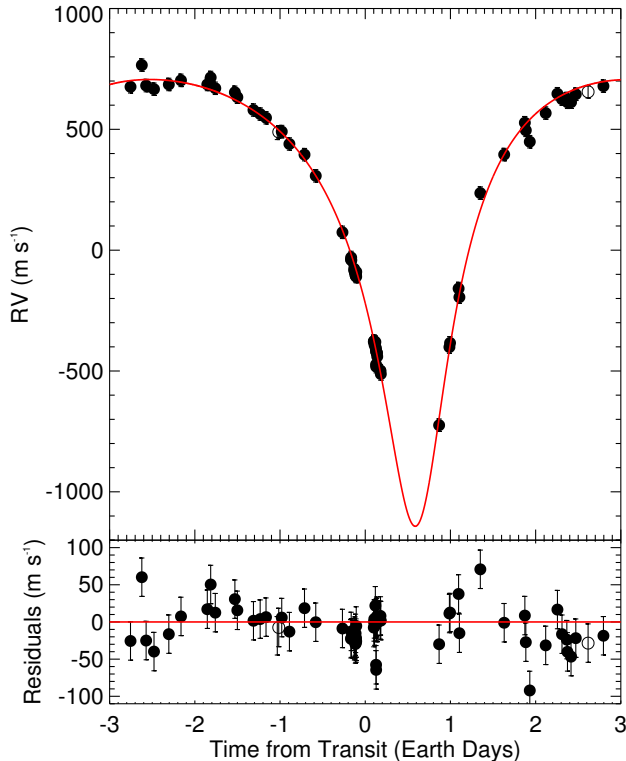


Figure 10. Top Panel: RV measurements for HAT-P-2 presented in Table 1 (black circles) folded with an orbital period equal to 5.6334729 d along with the best fit RV solution (red line) with long term variation in the RV signal due to substellar object c removed. Open circles represent RV measurements taken after the completion of the analysis. Bottom Panel: Residuals between the RV measurements and best fit solution. Error bars on the data points include the best-fit stellar jitter term (σ_{jitter}).

et al. 2008). The ‘prayer-bead’ errors are typically 1.5–3 \times larger than the errors determined from our MCMC analysis. The largest increases in the uncertainty using the ‘prayer-bead’ method were for the planet-star ratio and secondary eclipse depths. In some cases the ‘prayer-bead’ errors are slightly smaller ($\sim 0.9\times$) than the errors from the MCMC analysis. In those cases we report the larger errors from the MCMC analysis. Table 2 presents the best-fit parameters for our data sets and their 1 σ error bars. We find that our photometric errors, σ_{phot} , are 1.05, 1.11, 1.11, and 1.15 times higher than the predicted photon noise limit at 3.6, 4.5, 5.8, and 8.0 μm respectively.

4. DISCUSSION

In the following sections we discuss the implications of these results for our understanding of the HAT-P-2 system and the atmospheric properties of HAT-P-2b. We compare our results with the previous studies of the HAT-P-2 system from Bakos et al. (2007b), Winn et al. (2007a), Loeillet et al. (2008), and Pál et al. (2010), which were limited to ground based transit and radial velocity data. We also compare our results to predictions from one-dimensional radiative transfer and semi-analytic models of HAT-P-2b’s atmosphere.

4.1. Orbital and RV Parameters

We find that our estimates for the orbital and RV parameters listed in Table 2 fall within the range of the values from previous studies presented in Table 3. We note that there is often a more than 3 σ discrepancy between orbital parameters for the HAT-P-2 system presented in previous studies (Table 3). We conclude that either previous studies underestimate their error bars for the discrepant parameters, or the planet’s orbital properties are varying in time. If we compare the orbital parameters we derived from the 3.6, 4.5, and 8.0 μm data sets, we find that our estimates are within 3 σ of each other. The previous studies presented in Table 3 included only ground-based transit and radial velocity data. By the inclusion of secondary eclipse in our data we were able to improve the estimate of the orbital eccentricity of HAT-P-2b by an order of magnitude over the value presented in Pál et al. (2010).

From our orbital and RV parameters we can estimate the mass of HAT-P-2b using

$$M_p = \frac{2\pi K \sqrt{1-e^2}}{P G \sin i} \left(\frac{a}{R_\star} \right)^2 R_\star^2, \quad (16)$$

where the orbital period (P) and stellar radius (R_\star) are assumed to be the values presented in Pál et al. (2010), 5.6334729 ± 0.0000061 d and $1.64^{+0.09}_{-0.08} R_\odot$ respectively. Values for the RV semi-amplitude (K), eccentricity (e), inclination (i), and normalized semi-major axis (a/R_\star) are taken as the error-weighted average of the values from the 3.6, 4.5, and 8.0 μm observations, which are presented in Table 4. We estimate the mass of HAT-P-2b to be $8.00 \pm 0.97 M_J$, which is within 1 σ of the previous estimates of M_p for HAT-P-2b (Table 3).

4.2. Linear RV Trend

Our RV data spans a period of nearly six years, which allows us to test for long term trends in the RV signal. We find a non-zero value for the linear term in our RV fit ($\dot{\gamma}$), which indicates the presence of a second body orbiting in the system. If we assume that this second companion to HAT-P-2 (‘c’) is on a circular orbit and is much less massive than its host star, we can relate $\dot{\gamma}$ to the mass and orbital semi-major axis of ‘c’ by the expression presented in Winn et al. (2009)

$$\dot{\gamma} \approx \frac{GM_c \sin i_c}{a_c^2}. \quad (17)$$

Figure 11 shows the range of values for $M_c \sin i_c$ and a_c that are allowed for the HAT-P-2 system given that $\dot{\gamma} = -0.0886 \pm 0.0030$. We know the orbital period of ‘c’ must be significantly longer than six years since we do not detect any significant curvature in our long term RV trend, so we set a lower limit of $M_c \sin i_c \sim 15 M_J$ and $a_c \sim 10$ AU based on an orbital period for ‘c’ of 24 years. We further employ adaptive optics imaging to search for ‘c’ and set an upper limit on the values of $M_c \sin i_c$ and a_c .

4.2.1. Adaptive Optics Imaging

In an attempt to directly image the body responsible for causing the linear RV trend, we observed HAT-P-2 on May 29, 2012 using NIRC2 (PI: Keith Matthews) and the Keck II adaptive optics (AO) system at Mauna

Table 3
Results from Previous HAT-P-2 Studies

Parameter	Bakos et al. (2007b)	Winn et al. (2007a)	Loeillet et al. (2008)	Pál et al. (2010)
<i>Transit Parameters</i>				
R_p/R_\star	0.0684±0.0009	0.0681±0.0036 ^a	0.06891 ^{+0.00090} _{-0.00086}	0.07227±0.00061
i (°)	>84.6	>86.8	90.0 ^{+0.85} _{-0.93}	86.72 ^{+1.12} _{-0.87}
a/R_\star	9.77 ^{+1.10} _{-0.02}	9.90±0.39 ^a	10.28 ^{+0.12} _{-0.19}	8.99 ^{+0.39} _{-0.41}
T_c (BJD-2400000)	54212.8563±0.0007	54212.8565±0.0006	...	54387.49375±0.00074
T_{14} (d)	0.177±0.002	0.1787±0.0013
T_{12} (d)	0.012±0.002	0.0141 ^{+0.0015} _{-0.0012}
<i>Secondary Eclipse Parameters</i>				
ϕ_{sec}	0.1847±0.0055 ^a	0.1969±0.0040 ^a	0.1896±0.0016 ^a	0.1868±0.0019
T_{14} (d)	0.1650±0.0034
T_c (BJD-2400000)	54388.546±0.011
<i>Orbital & RV Parameters</i>				
P (d)	5.63341±0.00013	5.63341 (fixed)	5.63341 (fixed)	5.6334729±0.000061
$e \cos \omega$	-0.5152±0.0036
$e \sin \omega$	-0.0441±0.0084
e	0.520±0.010	0.501±0.007	0.5163 ^{+0.0025} _{-0.0023}	0.5171±0.0033
ω (°)	179.3±3.6	187.4±1.6	189.92 ^{+1.06} _{-1.20}	185.22±0.95
T_p (BJD-2400000)	54213.369±0.041	...	54213.4798 ^{+0.0053} _{-0.0030}	...
K (m s ⁻¹)	1011±38	883±57 ^a	966.9±8.3	983.9±17.2
<i>Planetary Parameters</i>				
M_p (M_J)	9.04±0.50	8.04±0.40	8.62 ^{+0.39} _{-0.55}	9.09±0.24
R_p (R_J)	0.982 ^{+0.038} _{-0.105}	0.98±0.04	0.951 ^{+0.039} _{-0.053}	1.157 ^{+0.073} _{-0.062}
ρ_p (g cm ⁻³)	11.9 ^{+4.8} _{-1.6}	10.60±0.55 ^a	12.5 ^{+2.6} _{-3.6}	7.29±1.12
g_p (m s ⁻²)	227 ⁺⁴⁴ ₋₁₆	207±20 ^a	237 ⁺³⁰ ₋₄₁	168±17
a (AU)	0.0677±0.0014	0.0681±0.0014 ^a	0.0677 ^{+0.0011} _{-0.0017}	0.06878±0.00068
<i>Noise Parameters</i>				
σ_{jitter} (m s ⁻¹)	60	31	17	...

^a Parameter value not directly quoted in reference, but calculated from quoted parameter values and errors

Table 4
HAT-P-2b parameters from a weighted average of the values from the 3.6, 4.5, and 8.0 μm fits

Parameter	Value
R_p/R_\star	0.06933±0.00045
E_{transit} (BJD)	2455288.84923±0.00037
a/R_\star	8.70±0.19
i (°)	85.97 ^{+0.28} _{-0.25}
e	0.50910±0.00048
ω	188.09±0.39
ϕ_{sec}	0.19253±0.00018
E_{sec} (BJD)	2455289.93211±0.00066
E_{periapse} (BJD)	2455289.4721±0.0038
M_p (M_J)	8.00±0.97
R_p (R_J)	1.106±0.061
ρ_p (g cm ⁻³)	7.3±1.6
g_p (m s ⁻²)	162±27
a (AU)	0.0663±0.0039

Kea (Wizinowich et al. 2000). Our observations consist of dithered images taken with the K' ($\lambda_c = 2.12\mu\text{m}$) filter. Using the narrow camera setting, which provides fine spatial sampling of the NIRC2 point-spread-function (10 mas pix⁻¹), we acquired 9 frames each having 13.2 seconds of on-source integration time. The seeing was estimated to be 0.4'' at visible wavelengths at the time of observations using AO wavefront sensor telemetry. We note that significant wind-shake degraded the quality of correction for some images but by only a

marginal amount.

The data were processed using standard techniques to correct for hot pixels, remove background radiation from the sky and instrument optics, flat-field the array, and align and co-add individual frames. Figure 12 shows the final reduced AO image along with the corresponding (10 σ) contrast levels achieved as a function of angular separation. No companions were detected in raw or processed frames.

We can use the limits from a non-detection to rule out the presence of companions as a function of $M_c \sin(i_c)$ and a_c . Using HAT-P-2's parallax distance of $119 \pm 8\text{pc}$ and estimated age of 2.6 ± 0.5 Gyr as determined by Pál et al. (2010) through a combined isochrone, light curve, and spectroscopic analysis, we find that our diffraction-limited observations are sensitive to companions on the hydrogen-fusing boundary for separations beyond $\approx 1''$. Interior to this region, the combination of imaging and RV data eliminates most low-mass stars, though late-type M-dwarf tertiaries located at ~ 40 AU could cause the long-term Doppler drift yet simultaneously evade direct detection (Figure 11)

4.2.2. Orbital Evolution

The likely presence of an M/L/T/Y dwarf at an orbital distance, a_c , of 10 to 40 AU from HAT-P-2b lends credence to the possibility that HAT-P-2b owes its current orbit to a history of Kozai cycling (Kozai 1962) combined with long-running orbital decay generated by tidal

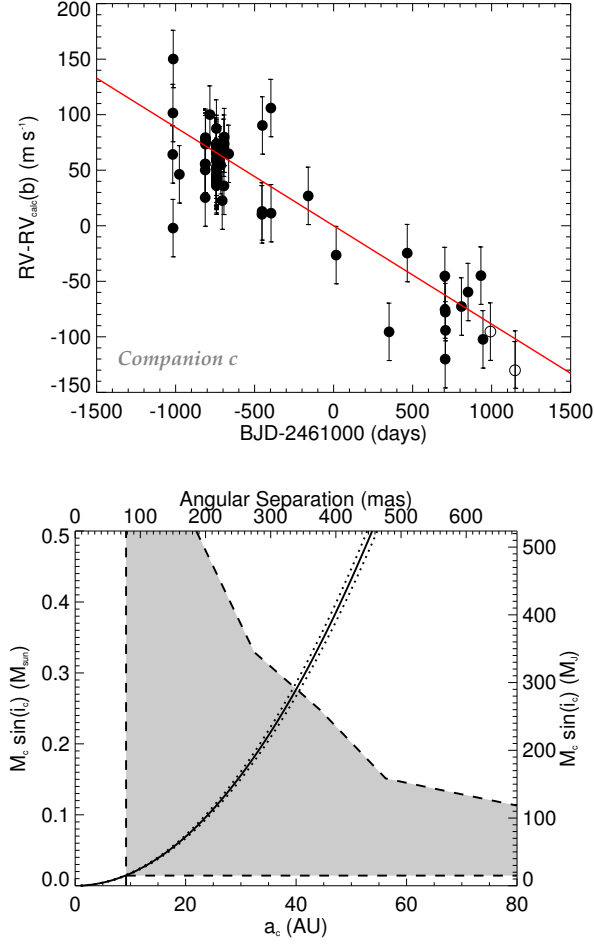


Figure 11. Top: RV variation as a function of BJD after subtracting the calculated variations due to HAT-P-2b. Red line shows our best-fit solution for the linear trend ($\dot{\gamma}$) in the data that result from companion ‘c’. Open circles represent RV measurements taken after the completion of the analysis, which conform with our measured linear trend. Bottom: Range of $M \sin i$ and semi-major axis (a) for companion ‘c’ (solid line) as estimated from the long term drift in the RV data ($\dot{\gamma}$). Dotted lines estimate the range in $M \sin i$ and a given the error in $\dot{\gamma}$. The shaded region gives the acceptable range of parameter space for companion ‘c’ given our upper and lower bounds on $M_c \sin i$ vs. a_c (dashed lines).

friction (Eggleton et al. 1998; Wu & Murray 2003; Fabrycky & Tremaine 2007). At first glance, this combination of Kozai Cycling and Tidal Friction (KCTF) seems more plausible than disk migration for producing the current orbital configuration of HAT-P-2b and indeed, long-distance disk migration for HAT-P-2b seems quite problematic. The protostellar disk itself would have needed to be exceptionally massive and long lived, and an ad-hoc mechanism must be invoked to explain the large observed orbital eccentricity of HAT-P-2b. Furthermore, HAT-P-2b has planetary and orbital parameters that place it significantly outside the well-delineated population of ‘conventional’ hot Jupiters with $P \sim 3$ days, $M \sim M_{\text{Jup}}$, and $e \sim 0$.

In the context of the KCTF process, HAT-P-2b is envisioned to have formed well outside its current orbit, perhaps via gravitational instability in the original protostellar disk. KCTF can operate if the mutual orbital inclination between companion ‘c’ and planet b was larger

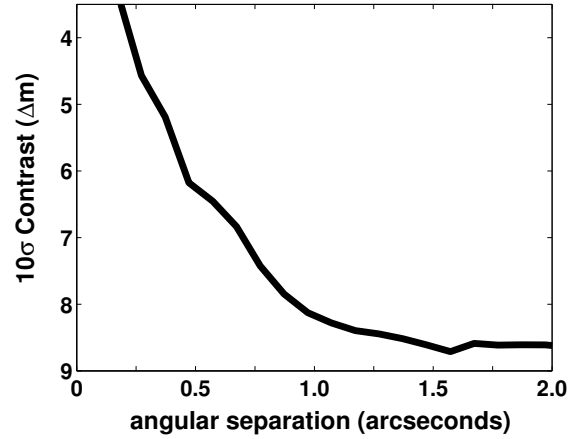
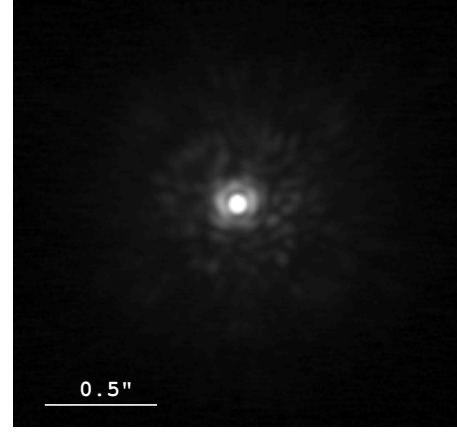


Figure 12. Left: Keck AO/NIRC2 K band image of the HAT-P-2 system. Image displayed using a square root scaling. Right: 10σ contrast limit for companion detection as a function of angular separation from which define the upper bounds on $M_c \sin i$ vs a_c .

(or better, substantially larger) than the Kozai critical angle, $i_c = \arccos[(3/5)^{1/2}] \sim 40^\circ$ (assuming $M_c \gg M_b$, and an initially circular orbit for b). In the event that KCTF did operate, planet b experienced periodic cycling between successive states of high orbital eccentricity and high mutual inclination. The timescale for these cycles was

$$\tau_{\text{Kozai}} = \frac{2P_c^2}{3\pi P_b} \frac{M_* + M_b + M_c}{M_c} (1 - e_c^2)^{3/2}. \quad (18)$$

With plausible values of $P_c = 25$ years, $e_c = 0.5$, and $M_c = 20M_{\text{Jup}}$, $\tau_{\text{Kozai}} = 300\text{Kyr}$. By contrast, the general relativistic precession rate for HAT-P-2b is currently

$$\omega_{\text{GR}} = \frac{3G^{3/2}(M_* + M_b)^{3/2}}{a_b^{5/2} c^2 (1 - e_b^2)}, \quad (19)$$

which generates a full 2π circulation of the apsidal line in 20 Kyr (τ_{GR}). Because $\tau_{\text{Kozai}} \gg \tau_{\text{GR}}$, the magnitude of the Kozai cycling is strongly suppressed at present.

To good approximation, tidal friction is currently the dominant contributor to the orbital evolution of HAT-P-2b, and it is plausible that the current state of the system has undergone dissipative evolution from an earlier epoch where $\tau_{\text{Kozai}} = \tau_{\text{GR}}$. If we assume that the tidal evolution has roughly conserved HAT-P-2b’s periastron distance, $d_{\text{peri}} = a_b(1 - e_b) = 0.033\text{AU}$, then in order for $\tau_{\text{Kozai}} = \tau_{\text{GR}}$ implies that HAT-P-2b has evolved to its current

orbit from an orbit with an initial period, $P_{o_{min}}$, given by

$$P_{o_{min}} = (1 - e_c^2)^{3/4} \frac{P_c M_\star}{c} \left(\frac{G}{M_c d_{peri}} \right)^{1/2}, \quad (20)$$

or

$$P_{o_{min}} \sim 33 \text{ d} \left(\frac{P_c}{25 \text{ yr}} \right) \left(\frac{20 M_{Jup}}{M_c} \right)^{1/2}. \quad (21)$$

Additionally, the radial velocity-derived constraint on the unseen companion ‘c’ indicates that $M_c \sim P_c^{4/3}$, which allows us to simply write

$$P_{o_{min}} \sim 33 \text{ d} \left(\frac{P_c}{25 \text{ yr}} \right)^{1/3}. \quad (22)$$

Given that direct imaging constrains the maximum period for companion ‘c’ to be of order 250 years, the KCTF scenario gives a lower limit on the possible initial periods for HAT-P-2b to be 30 days $< P_{o_{min}} < 60$ days.

The KCTF process delivers planets into orbits in which the planetary orbital angular momentum and the stellar spin angular momentum are initially largely uncorrelated. As mentioned earlier in the text, initial measurements of the projected spin-orbit misalignment angle, λ , suggested that HAT-P-2b’s orbit lies in the stellar equatorial plane. Recently, however, an reassessment by Albrecht et al. (2012) reports $\lambda = 9^\circ \pm 5^\circ$, indicating a modest projected misalignment. In addition, HAT-P-2b’s parent star is almost precisely on the $T_{\text{eff}} = 6250\text{K}$ boundary at which stars empirically appear to be able to maintain misalignment over multi-Gyr time scales (Albrecht et al. 2012).

4.3. Transit Timing Variations

We calculate ephemeris for the HAT-P-2 system given the center of transit and eclipse times presented in Table 2 as:

$$T_c(n) = T_c(0) + n \times P \quad (23)$$

where T_c is the predicted transit, eclipse, or periapse time and n is the number of orbits that have elapsed since $T_c(0)$. From our transit data we calculate $T_c(0) = 2455288.84923 \pm 0.00037$ BJD and $P = 5.6334754 \pm 0.0000026$ d, which is consistent with the orbital period for HAT-P-2b presented in Pál et al. (2010). We calculate $T_c(0) = 2455289.93211 \pm 0.00066$ BJD and $P = 5.6334830 \pm 0.0000086$ d from our secondary eclipse data and $T_c(0) = 2455289.4721 \pm 0.0038$ BJD and $P = 5.633479 \pm 0.000026$ d from our estimated times of periapse passage. The orbital periods estimated from the secondary eclipse and periapse passage timings are within 1σ of the value derived from our transit timings. Figure 13 presents our transit, secondary eclipse, and periapse times compared to our derived constant ephemeris. We define the center of transit/eclipse to occur when the projected planet-star distance given by Equation 3 is minimized. The definition of transit/eclipse center is not always clearly stated in studies for eccentric systems. Pál et al. (2010) estimate a difference between RV and photometric transit centers for the HAT-P-2 system of nearly two minutes. Some of the spread in the measured vs. predicted transit times could be accounted for by inconsistent definitions of transit center.

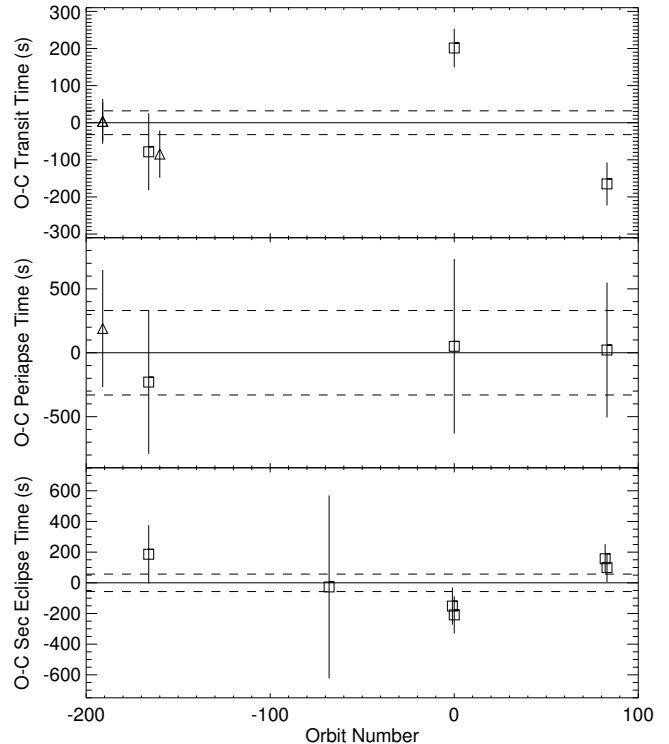


Figure 13. Observed minus calculated transit (top panel), periapse passage (middle), and secondary eclipse (bottom panel) times from data presented in Tables 2 (squares) and 3 (triangles). Dashed lines indicate the 1σ uncertainties in the predicted transit, periapse, and eclipse times. The variation that we see in the transit times

The separate visits to HAT-P-2b for the 3.6, 4.5, 5.8, and 8.0 μm observations allow constraints to be placed on possible transit timing variations (TTV) for HAT-P-2b. Previous transit timing measurements for this system (Bakos et al. 2007b; Winn et al. 2007a; Pál et al. 2010) had relatively low timing resolution ($\Delta t \sim 50 \rightarrow 500$ s) and appeared to be consistent with a constant ephemeris (Pál et al. 2010). Somewhat surprisingly, the *Spitzer* data from orbits 0 and 83 appear to be inconsistent with a constant ephemeris at the $\sim 3.5\sigma$ level, with a typical deviation of 150 s. The deviations are anti-correlated between primary transit and secondary eclipse, and they switch sign on the two successive visits. This could be due to either an astrophysical cause, or an as-yet unmodeled systematic error. In the sections below we consider two potential astrophysical explanations for the TTVs: a planetary satellite or an external perturber.

4.3.1. TTVs generated by a planetary satellite

HAT-P-2b is expected to be in pseudo-synchronous rotation, in which its spin period is close to the orbital frequency in the vicinity of periapse. Given $P_{\text{orbit}} = 5.63347$ d, Hut (1981)’s treatment gives

$$P_{\text{spin}} = \left[\frac{\frac{5e^6}{16} + \frac{45e^4}{8} + \frac{15e^2}{2} + 1}{(1 - e^2)^{3/2} \left(\frac{3e^4}{8} + 3e^2 + 1 \right)} \right]^{-1} P_{\text{orbit}} = 1.89 \text{ d}. \quad (24)$$

In order to maintain orbital dynamical stability, a

prospective moon for HAT-P-2b must have have an orbital semi-major axis, a_{sat} , such that $a_{\text{sat}} \lesssim F_{\text{crit}} R_{\text{Hill}}$, where R_{Hill} is the Hill Sphere radius at periapse,

$$R_{\text{Hill}} \sim a_{\text{pl}}(1 - e) \left(\frac{M_{\text{pl}}}{3M_{\star}} \right)^{1/3} = 0.0042 \text{ AU}, \quad (25)$$

and $F_{\text{crit}} \lesssim 0.5$ (see, e.g. Barnes & O'Brien (2002) for a discussion of satellite stability for planets with low orbital eccentricity). At distance $a_{\text{sat}} < F_{\text{crit}} R_{\text{Hill}}$ from HAT-P-2b, the orbital period of the satellite is $P_{\text{sat}} = 0.385 \text{ d}$, which is substantially shorter than the $P_{\text{spin}} = 1.89 \text{ d}$ spin period of the planet. Tidal evolution will therefore cause the satellite's orbit to gradually spiral in to meet the planet (Sasaki et al. 2012).

Based on the fairly uniform satellites-to-planet mass ratios exhibited by the regular satellites of the Jovian planets in the solar system, and in the absence of any concrete information regarding exomoons, it is not unreasonable to expect $M_{\text{sat}} = M_{\text{pl}}/10^4 \sim 0.28 M_{\oplus}$. The characteristic time for a satellite's orbital decay, assuming an equilibrium theory of tides with a frequency-independent tidal quality factor, Q_{p} , is (Murray & Dermott 1999)

$$\tau = \frac{2}{13} (F_{\text{crit}} R_{\text{Hill}})^{13/2} \frac{Q_{\text{pl}}}{3k_{2p} M_{\text{s}} R_{\text{pl}}^5} \left(\frac{M_{\text{pl}}}{G} \right)^{1/2}. \quad (26)$$

Adopting $Q_{\text{pl}} = 10^6$, and $k_{2p} = 0.1$ we find $\tau \sim 2 \text{ Gyr}$, which is comparable to the estimated stellar age, $\tau_{\star} = 2.7 \text{ Gyr}$ (Pál et al. 2010). The small value for the apsidal Love number, k_{2p} , stemming from the fact that HAT-P-2b at $8M_{\text{Jup}}$ is quite centrally condensed in comparison to Jupiter Bodenheimer et al. (see 2001); Batygin et al. (see 2009, for a discussion of the relation between k_{2p} and interior models). Given the substantial range of possible values for Q_{pl} , it would therefore not be unreasonable to find that HAT-P-2b harbors a fairly massive moon.

A moon with the above qualities would produce transit timing variations of magnitude (Kipping 2009)

$$\delta_{\text{TTV}_{\text{sat}}} = \frac{a_{\text{pl}}^{1/2} F_{\text{crit}} R_{\text{Hill}} M_{\text{sat}}}{M_{\text{sat}} + M_{\text{pl}} (2GM_{\star})^{1/2} \Lambda}, \quad (27)$$

where the geometric factor Λ appropriately amplifies or damps the transit timing variations in accordance with the eccentricity and orientation of the elliptical orbit of the planet about the parent star

$$\Lambda = \cos \left[\tan^{-1} \left(\frac{-e \cos(\omega)}{1 + e \sin \omega} \right) \right] \left(\frac{2(1 + e \sin \omega)}{1 - e^2} - 1 \right)^{1/2}. \quad (28)$$

Substituting the various values discussed above, we find

$$\delta_{\text{TTV}_{\text{sat}}} = 0.15 \text{ s}. \quad (29)$$

which is several orders of magnitude too small to be of current interest. So while (somewhat surprisingly) it is distinctly possible that HAT-P-2b could currently harbor a massive satellite, any such satellite cannot be responsible for transit timing variations of the size that appear to be present.

4.3.2. TTVs generated by an external perturber with a long period

Perturbations from an as-yet undetected perturbing body present another potential explanation for the apparent transit timing variations. After the signature of HAT-P-2b's orbit has been removed from the existing RV observations, a secular acceleration that can be attributed to a distant companion remains. The constancy of the acceleration implies an orbital period for the companion of at least several years; for example, a body with mass, $M_c \sim 18M_{\text{Jup}}$, and semi-major axis, $a_c = 10 \text{ AU}$, would suffice. For a configuration in which $a_c \gg a_{\text{pl}}$ (Holman & Murray 2005),

$$\delta_{\text{TTV}_{\text{perturber}}} \sim \frac{45\pi}{16} \frac{M_c}{M_{\star}} P_{\text{pl}} \alpha_e^3 (1 - \sqrt{2} \alpha_e^{3/2})^{-2}. \quad (30)$$

where $\alpha_e = a_{\text{pl}}/(a_c(1 - e_c))$. For a perturber with $M_c \sim 18M_{\text{Jup}}$, $e_c = 0.3$ and $a_c = 10 \text{ AU}$, we find $\delta_{\text{TTV}_{\text{perturber}}} = 0.1 \text{ s}$. In addition, direct numerical integrations indicate that for external perturbing planets that are consistent with the observed secular acceleration, the expected TTVs are invariably very small, and furthermore, do not exhibit the rapid variation shown by the timing reversal observed between orbit 0 and orbit 83.

4.3.3. A low-mass resonant perturber?

There are an effectively infinite number of stable orbits for perturbing bodies in mean-motion resonance with HAT-P-2b, and the diversity of such orbits is extended by HAT-P-2b's substantial eccentricity. A body in low-order resonance with HAT-P-2b can readily induce transit timing variations of the magnitude that are apparently observed, and *may* be able to produce the curious structure exhibited by the timing variations of the secondary eclipses and the primary transits. Exploratory calculations are currently underway to evaluate this possibility. If we assume that the observed TTV are generated by a gravitational perturber, this appears to be the most promising approach. However, we note that the significance of the reported transit timing variations is less than 4σ . Further high-precision transit and/or secondary eclipse observations along with additional RV measurements would be needed to confirm the presence of these TTVs and constrain the properties of the perturbing body.

4.4. Transit and Secondary Eclipse Depths

From our three transit observations we obtain planet-star radius ratios of 0.06821 ± 0.00075 , 0.07041 ± 0.00060 , and 0.0668 ± 0.0016 at 3.6, 4.5, and $8.0 \mu\text{m}$ respectively. Our estimates of the planet/star radius ratio, R_p/R_{\star} , are significantly smaller than the value presented in Pál et al. (2010), but are fairly well aligned with the values presented in Bakos et al. (2007b), Winn et al. (2007a), and Loeillet et al. (2008). Although Pál et al. (2010) incorporate the *I* band observations from Bakos et al. (2007b) they also include follow up observations that utilize the *z* and Strömgren *b + y* bandpasses. While the *I* and *z* bands probe a similar wavelength range ($\sim 0.8 - 0.9 \mu\text{m}$), the Strömgren *b* and *y* bands probe a slightly shorter wavelength range ($\sim 0.5 \mu\text{m}$) where atmospheric scattering may become important.

The difference between our values of R_p/R_{\star} at 3.6, 4.5, and $8.0 \mu\text{m}$ could point to enhanced atmospheric opacity in the $4.5 \mu\text{m}$ bandpass due to CO, but our values

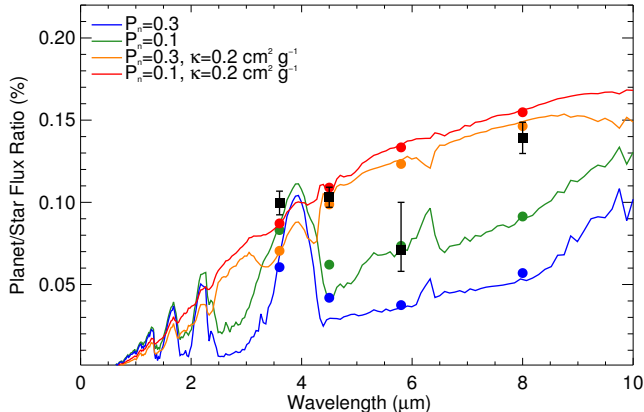


Figure 14. Secondary eclipse depths (squares) at 3.6, 4.5, 5.8, and 8.0 μm compared to one-dimensional atmosphere models for HAT-P-2b’s day side following Burrows et al. (2008) with the planet at a distance of 0.0478 A.U. The models presented here incorporated values of the parameterized recirculation parameter (P_n) of both 0.1 and 0.3 and allowed for the presence of a modest high-altitude absorber ($\kappa = 0.2 \text{ cm}^2 \text{ g}^{-1}$). Filled circles represent the band integrated planet/star flux ratio for each of the IRAC bands. Models with an inversion best match data at 3.6, 4.5, and 8.0 μm .

of R_p/R_\star differ by less than 2σ . Given the large value of the average gravitational acceleration of HAT-P-2b ($162 \pm 27 \text{ m s}^{-2}$, Table 4), we would expect atmospheric scale heights to be small, which supports our wavelength independent values for the planetary radius. If we assume a value of $R_\star = 1.64^{+0.09}_{-0.08} R_\odot$ (Pál et al. 2010), then we find an average radius value for HAT-P-2b of $R_p = 1.106 \pm 0.061 R_J$. The radius of planet, given its mass, is in line with models of the thermal evolution of massive strongly irradiated planets. Planetary radii of 1.13 to 1.22 R_J for 8 M_J planets are expected for 1-10 Gyr ages (Fortney et al. 2007).

The estimates for the secondary eclipse depths at 3.6, 4.5, 5.8, and 8.0 μm presented here are the first secondary eclipse measurements for HAT-P-2b. We compare these results to the predictions of atmospheric models for this planet to better understand the atmospheric properties of HAT-P-2b. Figure 14 presents predicted day side emission as a function of wavelength from a one-dimensional radiative transfer model similar to those described in Burrows et al. (2008). These models assume a solar-metallicity atmosphere in local thermochemical equilibrium and include a parameterization for the redistribution of heat from the day side to the night side of the planet (P_n) and the possible presence of a high-altitude optical absorber (κ). It is important to note that these one-dimensional models assume instantaneous radiative equilibrium and therefore do not account for the expected phase lag between the incident flux and planetary temperatures for eccentric planets.

Models that also include an additional high-altitude optical absorber to produce a dayside inversion best match our 3.6, 4.5, and 8.0 μm data points. We find some difficulty in matching the 5.8 μm data point. We note that even with our best attempts to remove the ramp from this data that the secondary eclipse depth appears to be slightly underestimated (Figure 8). Given the large uncertainty in the 5.8 μm secondary eclipse depth it is within 2.5σ of the flux ratio predicted by our mod-

els that include an inversion. Both the 4.5 and 8.0 μm secondary eclipse depths are more than 14σ larger than those predicted by atmospheric models without an inversion. Even if the planet were assumed to be $\sim 100 \text{ K}$ warmer to account for the phase lag in planet-wide temperatures, models without an inversion would still underestimate the planetary flux in the 4.5 and 8.0 μm bands.

We calculate brightness temperatures in each band using a PHOENIX stellar atmosphere model for the star (Hauschildt et al. 1999). The 3.6 μm eclipse depths have an average value of $0.0996\% \pm 0.0072\%$, which corresponds to a brightness temperature of $2392 \pm 84 \text{ K}$. We find an average 4.5 μm eclipse depth of $0.1031\% \pm 0.0061\%$ and a corresponding brightness temperature of $2117 \pm 65 \text{ K}$. Our eclipse depth at 5.8 μm corresponds to a brightness temperature of $1613^{+335}_{-150} \text{ K}$, while our eclipse depth at 8.0 μm corresponds to a brightness temperature of $2258 \pm 106 \text{ K}$. Our secondary eclipse measurements in the 3.6 and 4.5 μm bandpasses agree at the 1σ level, and therefore do not provide any convincing evidence for variability in the planet’s flux. Further observations of HAT-P-2b at 3.6 and 4.5 μm could place better constraints on possible orbit-to-orbit variability in the planet’s thermal structure.

4.5. Phase Curve Fits

The overall shape and timing of the maximum and minimum of the planetary flux from our phase curves reveals a great deal about the atmospheric properties of HAT-P-2b. For planets on circular orbits, phase curve observations are generally related to day/night brightness contrasts on the planet. In the case of HAT-P-2b, the phase variations in the planetary flux are more indicative of thermal variations that result from the time-variable heating of the planet. In both the circular and eccentric cases the thermal phase amplitude and phase lag are determined by the radiative and advective timescales of the planet. By comparing the 3.6, 4.5, and 8.0 μm phase variations we can gain further insights into the thermal, wind, and possible chemical structure of HAT-P-2b’s atmosphere.

We find that the peak of the observable planetary flux at 3.6 μm occurs 4.39 ± 0.28 hours after periapse passage with a peak value of $0.1139\% \pm 0.0089\%$, which corresponds to a brightness temperature of $2556 \pm 100 \text{ K}$. The exact timing and level of the minimum planetary flux at 3.6 μm is much more uncertain. We find the planetary flux at 3.6 μm drops below observable levels for a period of ~ 1 day $18.36^{+0.18}_{-1.0}$ hours before transit. As such we can only put an upper limit of 1040 K on the minimum brightness temperature of HAT-P-2b at 3.6 μm .

The observed 4.5 μm HAT-P-2b phase curve exhibits a peak in the observable planetary flux 5.84 ± 0.39 hours after periapse passage with a value of $0.1162\%^{+0.0089\%}_{-0.0071\%}$ and corresponding brightness temperature of $2255^{+92}_{-74} \text{ K}$. We detect emission from HAT-P-2b over the entirety of its orbit at 4.5 μm with a minimum in the planet/star flux ratio of $0.0372\%^{+0.0086\%}_{-0.0096\%}$, which corresponds to a brightness temperature of $1345^{+119}_{-133} \text{ K}$. This minimum in the planetary flux occurs 6.71 ± 0.43 hours after transit. Roughly speaking, the shift of the minimum of the observed phase curve at 4.5 μm away from region be-

tween apoapse and transit points to a minimum in the planetary temperature that is shifted west from the anti-stellar longitude and/or that the nightside of the planet is still cooling even after the transit event. We would expect the planet to have a temperature minimum east of the anti-stellar point near the sunrise terminator assuming a super-rotating flow as shown for HD 189733b and HD 209458b in Showman et al. (2009). This dip in the planetary flux after transit is indeed puzzling and will be investigated further in a future study.

Our 8.0 μm observations cover only the portion of HAT-P-2b’s orbit between transit and secondary eclipse, so we can only constrain the behavior of the 8.0 μm phase curve near the peak of the planetary flux. We find that the peak in the planetary flux at 8.0 μm occurs 4.64 ± 0.33 hours after the predicted time for periapse passage. The maximum of the planetary flux at 8.0 μm is $0.1888 \pm 0.0072\%$, which corresponds to a brightness temperature of 2806 ± 79 K.

It is significant that we obtain a good fit to the data using Equation 12, which is similar to the functional form used to fit the light curves of HD 189733b and WASP-12b in Knutson et al. (2012) and Cowan et al. (2012a) respectively and produce a longitudinal map of the planet’s thermal variations. The “longitudinal” direction of thermal phase maps, ϕ , must be understood to mean “local stellar zenith angle”, Φ . Thermal phase variations probe the diurnal cycle, $T(\Phi)$. A tidally-locked planet has 1-to-1 correspondence between local stellar zenith angle and longitude (e.g.: $\phi = \Phi$), but phase maps can be made regardless of rotation rate (e.g., for Earth Cowan et al. 2012b).

Nonetheless, there are two reasons that phase mapping should not work for eccentric planets: 1) the time-variable incident flux makes the brightness map time-variable ($T(\Phi, t)$), and 2) the time-variable orbital angular velocity of the planet dictates that longitudinally sinusoidal variations in brightness on the planet would not correspond to sinusoidal variations in the light curve. Equation 12 is sinusoidal in the true anomaly (f) rather than in time, which implicitly accounts for 2).

The fact that Equation 12 fits the phase variations of HAT-P-2b implies that the diurnal brightness profile of the planet is constant throughout the orbit: $dT(\Phi)/dt = 0$. This is entirely different from claiming that the longitudinal brightness profile of the planet is constant: since the planet is on an eccentric orbit, there is no fixed correspondence between longitude and stellar zenith angle. Rather, our data seem to indicate that the planet maintains a constant brightness as a function of stellar zenith angle, in marked disagreement with expectations for such an eccentric planet. This is almost certainly due to a geometric coincidence, however: HAT-P-2b shows us its day-side shortly after periapse. The day-side brightness of the planet likely changes throughout its orbit, but we are not privy to it.

4.5.1. Interpreting the Flux Maximum

We use the semi-analytic model developed in Cowan & Agol (2011) to interpret the peak amplitudes and phase lags of the planet’s thermal brightness variations. This is essentially a two-dimensional, one-layer energy balance model where the user specifies Bond albedo, radiative timescale at the sub-stellar point at periapse, and the

characteristic zonal¹ wind velocity.

The Bond albedo is assumed to be 0.1 for all of the simulations shown here. Measured albedos of hot Jupiters range from 0.025 for TrES-2b (Kipping & Spiegel 2011) to 0.32 for Kepler-7b (Demory et al. 2011). Since HAT-P-2b is viewed equator-on, its albedo is degenerate with poleward heat transport, which we do not explicitly model. Increasing either albedo or meridional² energy transport has the effect of uniformly decreasing the planet’s flux throughout its orbit.

The sub-stellar radiative timescale is specified at periapse, and is assumed to scale as $\tau_{\text{rad}} \propto T^{-3}$ (Showman & Guillot 2002; Showman et al. 2010), as one would expect for blackbody parcels of gas. The radiative relaxation time therefore varies throughout the orbit and is also a function of the location of a parcel of gas on the planet.

Observationally, the zonal wind speeds on a gas giant like HAT-P-2b are degenerate with its rotation rate. In our model we therefore specify the angular velocity of gas parcels in an inertial frame, rather than in the usual rotating planet frame. By adopting the Hut (1981) prescription for pseudo-synchronous rotation of binary stars, we convert the inertial angular frequency into an equatorial zonal wind speed in the rotating planet’s frame. If another prescription is more appropriate for the planet’s rotation rate (e.g. Ivanov & Papaloizou 2007), then the equatorial wind velocities presented here are off by a uniform offset.

Both zonal wind speeds and albedo are assumed to be constant throughout the planet’s orbit. The constant zonal wind velocity is likely the most problematic assumption given that three-dimensional simulations of Kataria et al. (2012) predict that zonal wind speeds at the mid-IR photosphere (pressures of 0.1-1 bar) change by tens of percent throughout the orbit of a hot Jupiter with an eccentricity of 0.5. It is also likely that the amount of equator-to-pole heat transport, which is degenerate with albedo in our model, will vary throughout HAT-P-2b’s orbit. Our assumption of a constant albedo for the planet could also be limiting given that clouds could form near the apoapse of HAT-P-2b’s orbit, then dissipate near periapse (Kane & Gelino 2010). By focusing on the region near periapse we limit the possible influence of temporal changes in albedo and wind speeds on our results.

4.5.2. Model of HAT-P-2b and Circular Analog

The top panels of Figure 15 shows how τ_{rad} and v_{wind} affect the 4.5 μm peak flux ratio and phase lag for HAT-P-2b. The dependencies are qualitatively similar for the other two wavebands. For comparison, we also show in bottom panels of Figure 15 the same dependencies for a hypothetical circular twin to HAT-P-2b with semi-major axis fixed at the actual planets periapse separation. There are a number of conclusions we can draw from these models:

1. For circular planets, the radiative time scale and wind velocity are entirely degenerate: both the peak flux ratio and the phase lag depend solely on the product $\tau_{\text{rad}} v_{\text{wind}} \propto \epsilon$, the ‘advective efficiency’ of Cowan & Agol (2011). Furthermore,

¹ zonal refers to the east/west direction

² meridional refers to the north/south direction

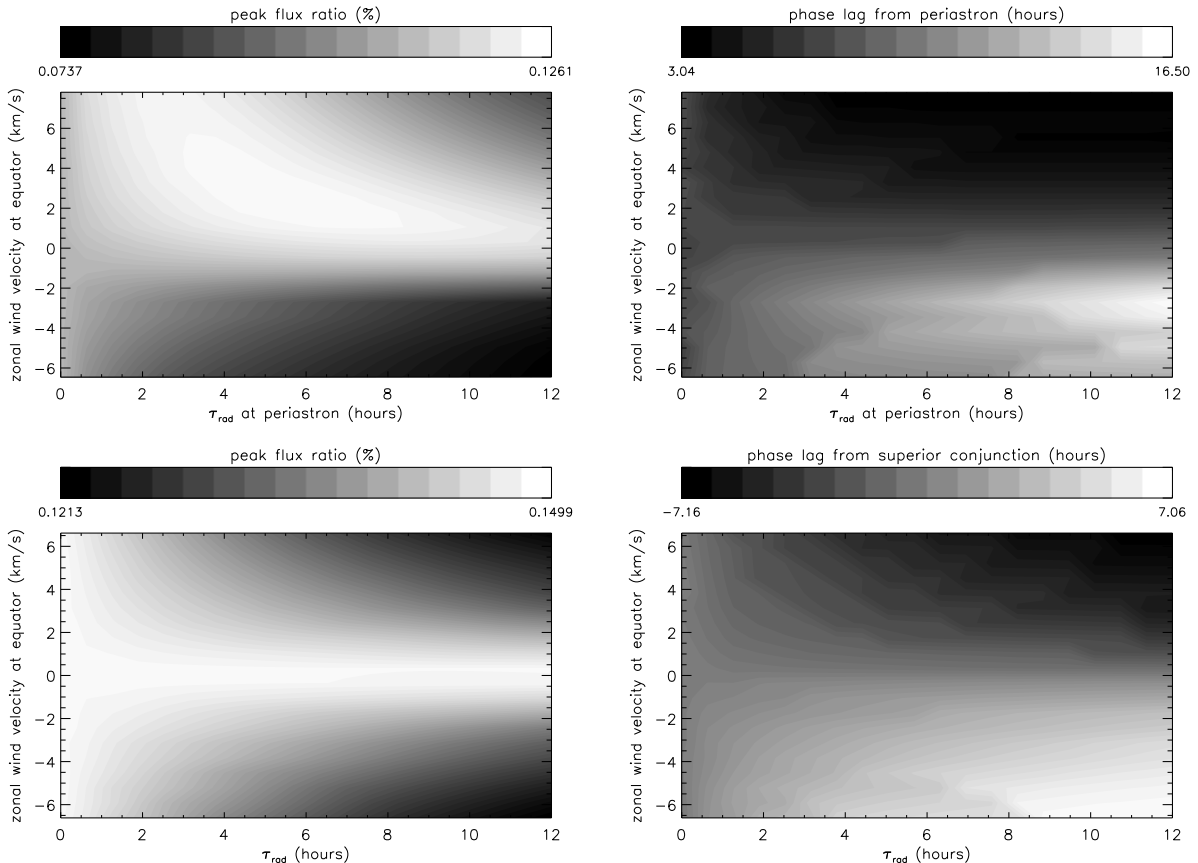


Figure 15. The dependence of peak flux ratio and phase lag at $4.5 \mu\text{m}$ on radiative timescale and zonal wind speed. The top panels are for HAT-P-2b; the bottom panels are for a hypothetical twin on a circular orbit with semi-major axis fixed at the periapse separation of HAT-P-2b. The plots were generated by computing $4.5 \mu\text{m}$ lightcurves on a 20×20 grid in τ_{rad} and v_{wind} using the energy balance model of Cowan & Agol (2011).

the peak flux does not depend on the direction of zonal winds. The phase lag, on the other hand, would have the same amplitude but opposite sign for eastward vs. westward zonal winds.

- The peak flux ratio for the eccentric planet HAT-P-2b depends approximately on the advective efficiency, ϵ , as for circular planets, but the dependence is no longer monotonic. The peak flux ratio exhibits a maximum for radiative times of ~ 6 hours and wind velocities of 2 km s^{-1} . This is because eastward advection of heat brings the hot spot into view shortly after periapse, as discussed in Cowan & Agol (2011). There is a local minimum in peak flux for $\tau_{\text{rad}} = 0$, the radiative equilibrium case. The global minimum, however, still occurs in the limit of long radiative times and rapid winds, which results in a planet with zonally uniform, time-constant temperature, as in the circular case.
- Comparing the top-right and bottom-right panels of Figure 15 shows that zonal winds have qualitatively the same effect, regardless of orbital eccentricity: eastward winds make the peak flux occur early, while westward winds cause a delay in the peak flux. The major difference between the two geometries is the phase-lag expected in the absence of winds, the null hypothesis. For a circular,

tidally-locked planet there is no phase lag in this limit, whereas the eccentric planet exhibits a large positive phase lag in the absence of winds. As a result of this different zero-point, the amplitude of phase lag *from periapse* decreases nearly monotonically for increasing ϵ in the eccentric model, exactly the opposite behavior from a circular planet. Such counter-intuitive behavior is precisely why it is more useful to compare phase lags to the windless scenario rather than quote absolute phase lags from periapse (Cowan & Agol 2011).

4.5.3. Constraints on Model Parameters

In Figure 16 we show exclusion diagrams in the v_{wind} vs. τ_{rad} plane for each waveband. Since we use a one-layer model, this can roughly be thought of as constraining the properties of the photospheres at each waveband, with the understanding that the mid-IR vertical contribution functions span approximately a factor of ten in pressure (e.g. Knutson et al. 2009b; Showman et al. 2009). Blue lines in Figure 16 show the 1 and 2σ confidence intervals from the peak flux value. Red lines show the same for the phase offset. Grayscale shows the combined confidence intervals.

At 3.6 and $4.5 \mu\text{m}$, the peak fluxes are consistent with a broad range of eastward zonal wind scenarios. Only very high values of ϵ (top-right of plot) and most westward winds (bottom of plot) are excluded. At $8 \mu\text{m}$,

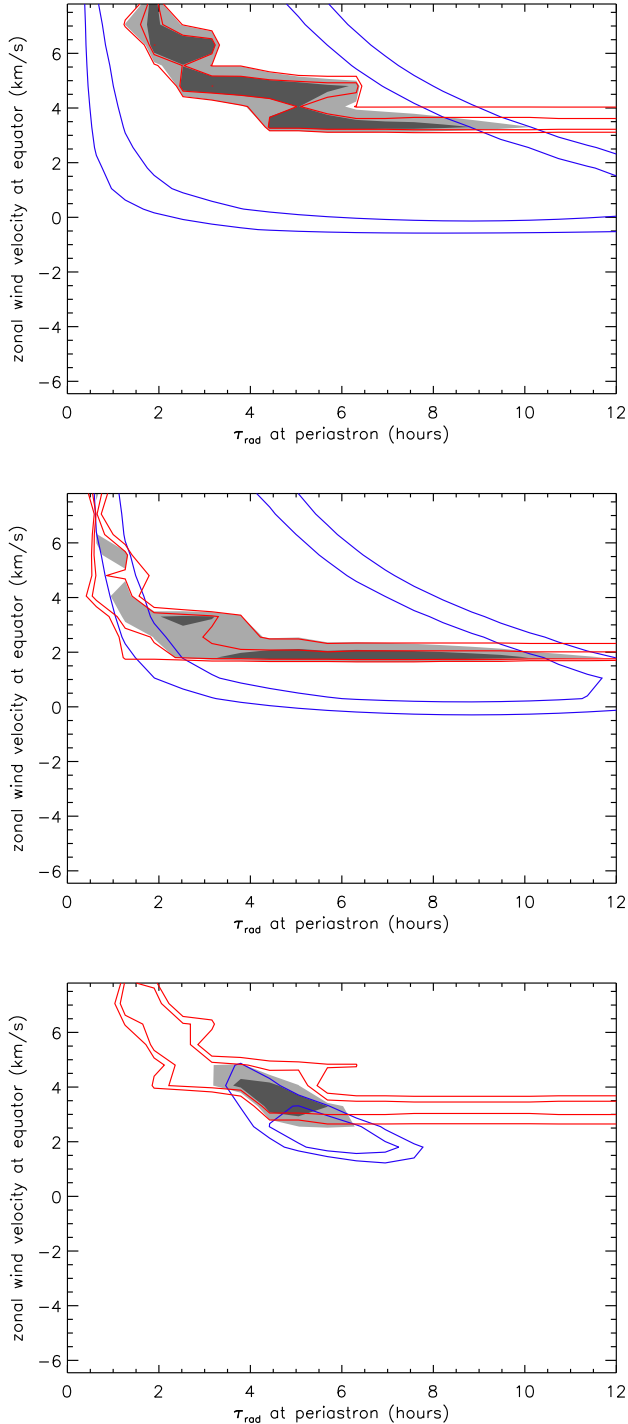


Figure 16. Exclusion diagrams for 3.6, 4.5, and 8.0 μm phase peaks. The blue lines show the one and two sigma confidence intervals based on the observed peak flux. Red lines show the same for the observed phase lag. Grayscale shows the combined constraint. The plots were generated by computing lightcurves on a 20×20 grid in τ_{rad} and v_{wind} using the energy balance model of Cowan & Agol (2011).

only the highest peak flux values are favored, but even these are a very poor fit. If we adopt a Bond albedo of zero, the 8 μm peak flux still disagrees with any models by $> 5\sigma$. We therefore conclude that the high flux at 8 μm is not due solely to atmospheric dynamics, but also to chemistry and the planet’s vertical temperature profile. This waveband falls within a water vapor absorption feature and is therefore expected to originate higher up in the atmosphere than either the 3.6 and 4.5 μm flux. The high flux in the 8.0 μm channel therefore suggests a temperature inversion, which is also supported by our measured secondary eclipse depths in Section 4.4.

The constraints from the phase lag of peak flux (red lines in Figure 16) are stronger, albeit still degenerate. The data favor a narrow range of advective efficiencies ($\tau_{\text{rad}}v_{\text{wind}}$). The bottom panel of Figure 16 gives the impression that the peak flux and phase lag at 8 μm combine to give a nice constraint on the model parameters, but the peak flux constraints should be taken with a grain of salt, as described above. It is important to note the decaying exponential-like trend of the preferred values of the zonal wind speeds with τ_{rad} in Figure 16 that pairs short values for τ_{rad} with higher values for v_{wind} and longer values for τ_{rad} with lower values for v_{wind} . Three-dimensional models that consistently couple radiative and advective processes will help to further constrain the relevant timescales in HAT-P-2b’s atmosphere over the full range of its orbit.

5. CONCLUSIONS

In this paper we present the first secondary eclipse and phase curve observations for the eccentric hot Jupiter HAT-P-2b in the *Spitzer* 3.6, 4.5, 5.8, and 8.0 μm bandpasses. These data include two full-orbit phase curves at 3.6 and 4.5 μm , a partial-orbit phase curve at 8.0 μm , three transit events, and six secondary eclipse events. The timing between transit and secondary eclipse during a single planetary orbit combined with radial velocity measurements allows us to better constrain the eccentricity ($e = 0.50910 \pm 0.00048$) and argument of periapse ($\omega = 188.09^\circ \pm 0.39^\circ$) of HAT-P-2b’s orbit. Long-term linear trends in the RV data indicate the presence of a third body in the system.

A comparison of our secondary eclipse depths with a one-dimensional model for the day-side emission of the planet suggests the presence of a day-side inversion in HAT-P-2b’s atmosphere. The timing and magnitude of the peak in the planetary flux at 3.6, 4.5, and 8.0 μm are explained by a range of advective and radiative parameters in our two-dimensional energy balance model, but suggest the presence of strong eastward equatorial winds ($\sim 2 - 6 \text{ km s}^{-1}$) and short radiative timescales ($\sim 2 - 8$ hours) at mid-IR photospheric levels near periapse.

Further work is needed to fully explain our observations of HAT-P-2b. Three-dimensional atmospheric models that couple radiative and advective processes and include a range of compositions would help to further explain the phase variations we observe for HAT-P-2b, especially outside of the orbital region near periapse. Additionally, low-resolution spectroscopy taken during secondary eclipse would help to better constrain the atmospheric chemistry of HAT-P-2b. Exoplanets on highly eccentric orbits like HAT-P-2b present observers and mod-

elers with a unique opportunity to disentangle the contributions of radiative, advective, and chemical processes at work in hot Jupiter atmospheres. By refining our understanding of exoplanets like HAT-P-2b we will be able to use that knowledge to better understand the atmospheric processes at work in other exoplanet atmospheres.

This work is based on observations made with the *Spitzer Space Telescope*, which is operated by the Jet Propulsion Laboratory, California Institute of Technology, under a contract with NASA. Support for this work was provided by JPL/Caltech. N.K.L. was further supported by NASA Headquarters under the NASA Earth and Space Science Fellowship Program (NNX08AX02H),

Origins Program (NNX08AF27G), and in part under contract with the California Institute of Technology (Caltech) funded by NASA through the Sagan Fellowship Program executed by the NASA Exoplanet Science Institute. Some of the data presented herein were obtained at the W.M. Keck Observatory, which is operated as a scientific partnership among the California Institute of Technology, the University of California and the National Aeronautics and Space Administration. The Observatory was made possible by the generous financial support of the W.M. Keck Foundation. N.K.L. wishes to thank B. K. Jackson and J. A. Carter for many useful discussions during the preparation of this manuscript and the anonymous referee for their helpful suggestions.

APPENDIX

NOISE PIXEL PARAMETER

The IRAC Point Response Function (PRF) results from the convolution of the stellar Point Spread Function (PSF) with the Detector Response Function (DRF). The shape of the PRF is not constant and varies with the DRF at each stellar centroid position and with changes in the stellar PSF determined by the optics. The shape of the PRFs differs substantially in each channel of the IRAC instrument as shown in Figure 17. Given this change in the shape of the PRF with wavelength, we expect that different methods to determine the stellar centroid position and correct for systematic effects may be needed in each of the four IRAC bands. Both the 3.6 and 4.5 μm channels of the IRAC instrument are shortward of the *Spitzer* 5.5 μm diffraction limit (Gehrz et al. 2007) and exhibit undersampled PRFs whose shape changes as the stellar centroid moves from the center to the edge of a pixel causing intrapixel sensitivity variations. The PRFs in the 5.8 and 8.0 μm channels of the IRAC instrument exhibit a more Gaussian-like shape that is better sampled by the detector resulting in only small intrapixel sensitivity variations.

Ideally, we would like to account for these changes in the PRF in our photometric measurements. We cannot make a direct determination of the exact shape of the PRF as a function of pixel position, but we can measure the normalized effective-background area of the PRF ($\tilde{\beta}$), which is also called noise pixels by the IRAC Instrument Team. If we assume the measured flux in a given pixel (F_i) is given by

$$F_i = F_0 P_i \quad (\text{A1})$$

where F_0 is the point source flux and P_i is PRF in the i^{th} pixel. The noise pixel parameter, $\tilde{\beta}$, is given by

$$\tilde{\beta} = \frac{(\sum F_i)^2}{\sum (F_i^2)} = \frac{(\sum F_0 P_i)^2}{\sum (F_0 P_i)^2} = \frac{(\sum P_i)^2}{\sum (P_i^2)} \quad (\text{A2})$$

since F_0 can be assumed to be constant. The numerator in Equation A2 is simply the square of the PRF volume (V) and the denominator is the effective background area (β). These quantities are related to the sharpness parameter, S_1 , first introduced by Muller & Buffington (1974) for constraining adaptive optics corrections by

$$\tilde{\beta} = \beta V^2 = \frac{1}{S_1}. \quad (\text{A3})$$

The S_1 parameter describes the ‘sharpness’ of the PRF and can range from zero (flat stellar image) to one (all the stellar flux in the central pixel).

As discussed in Mighell (2005), the S_1 parameter is related to the standard deviation (σ) of the PRF by

$$S_1 = \frac{1}{C_1 \sigma^2} \quad (\text{A4})$$

where C_1 is a constant that depends on the sampling of the PRF on the detector. From Equations A4 and A3 it can be shown that

$$\sigma \propto \sqrt{\tilde{\beta}}. \quad (\text{A5})$$

For both the 3.6 and 4.5 μm data we measure $\tilde{\beta}$ with the same circular aperture sizes used to determine the stellar centroid position.

We find that $\tilde{\beta}$ can serve two purposes in improving the signal-to-noise of the 3.6 μm observations. First, using a circular aperture with a radius proportional to $\sqrt{\tilde{\beta}}$ reduces the overall variations in raw unbinned flux from $\sim 5\%$ to $\sim 2\%$. Harris (1990) and Pritchett & Kline (1981) note that the optimal aperture radius for a circularly-symmetric Gaussian with a standard deviation of σ is $r_0 \approx 1.6 \sigma$, which is similar to our optimal aperture radius $r_0 \approx \sigma \approx \sqrt{\tilde{\beta}}$.

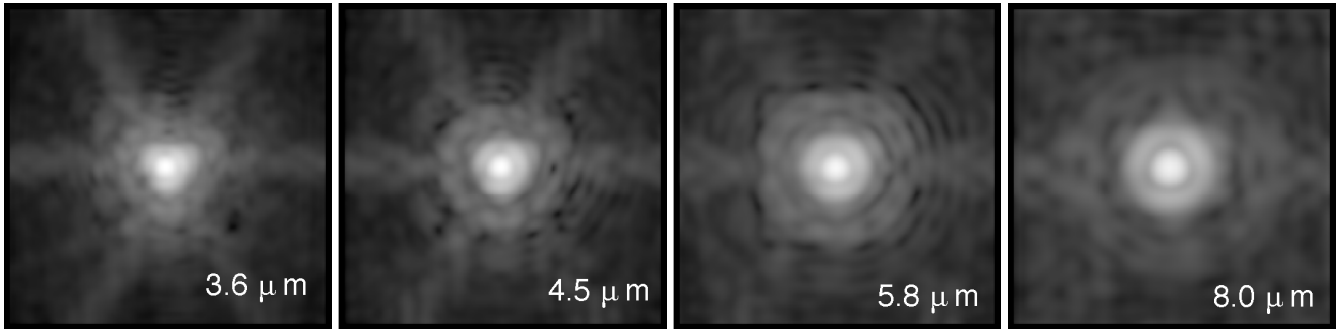


Figure 17. *Spitzer* IRAC point response functions (PRFs) at 3.6, 4.5, 5.8, and 8.0 μm . The PRFs were generated by the IRAC team from bright calibration stars observed at several epochs. The PRFs are displayed using a logarithmic scaling to highlight the differences in the PRFs in each bandpass.

Second, we find that using $\sqrt{\tilde{\beta}}$ as an additional spatial constraint in the intrapixel sensitivity correction at 3.6 μm can improve the accuracy, as defined by the standard deviation of the residuals, in our final solution by $\sim 1\text{-}2\%$. We find that using $\tilde{\beta}$ as an additional constraint for the 4.5 μm observations does not significantly improve the accuracy of our results. This is not surprising since the IRAC 4.5 μm channel is closer to the *Spitzer* diffraction limit of 5.5 μm (Gehrz et al. 2007). We also find that $\tilde{\beta}$ does not vary with stellar centroid position in the 5.8 and 8.0 μm observations, which are longward of the *Spitzer* of the diffraction limit.

INTRAPIXEL SENSITIVITY CORRECTION

The 3.6 and 4.5 μm channels of the *Spitzer* IRAC instrument both exhibit variations in the measured flux that are strongly correlated with the position of the star on the detector (Figures 1 and 2). These flux variations are the result of well documented intrapixel sensitivity variations that are exacerbated by an undersampled PRF (e.g., Reach et al. (2005), Charbonneau et al. (2005, 2008), Morales-Calderón et al. (2006), Knutson et al. (2008)). The most common method used to correct intrapixel sensitivity induced flux variations is to fit a polynomial function of the stellar centroid position (Reach et al. 2005; Charbonneau et al. 2005, 2008; Morales-Calderón et al. 2006; Knutson et al. 2008). This method works reasonably well on short timescales (< 10 hours) where the variations in the stellar centroid position are small (< 0.2 pixels). Recently, studies by Ballard et al. (2010) and Stevenson et al. (2011) have implemented non-parametric corrections for intrapixel sensitivity variations by creating pixel ‘maps’, which give a smaller scatter in the residuals compared with parametric models in most cases.

The pixel mapping method of Ballard et al. (2010) uses a Gaussian low-pass spatial filter to estimate the weighted sensitivity function given by

$$W(x_i, y_i) = \frac{\sum_{j \neq i}^n K_i(j) \times F_{0,j}}{\sum_{j \neq i}^n K_i(j)} \quad (\text{B1})$$

where

$$K_i(j) = \exp\left(-\frac{(x_j - x_i)^2}{2\sigma_x^2} - \frac{(y_j - y_i)^2}{2\sigma_y^2}\right) \quad (\text{B2})$$

$F_{0,j}$ is the stellar flux measured in the j th frame, x_j/y_j and x_i/y_i are the stellar centroid position in the j th and i th image respectively, and σ_x and σ_y are the widths of the Gaussian filter in the x and y directions. In the Ballard et al. (2010) study, they assumed that all observations obtained outside of planetary transit ($F_{0,j}$) represented the intrinsic stellar flux (F_0) convolved with the intrapixel sensitivity function. In our study, we must account for possible variations in the flux from the HAT-P-2 system due to phase variations in the flux from HAT-P-2b. This requires us to iteratively solve Equation B1, where $F_{0,j}$ is determined at each step by removing a model for the planetary transit, eclipse, and phase variations from the observed flux (F_j).

The main challenge in applying the Ballard et al. (2010) method to the HAT-P-2 data set is that as the number of data points, n , becomes large the time required to compute Equation B1 over the full data set becomes prohibitively long. We must iteratively solve Equation B1 to constrain the phase variations of the planet, which requires the summation over n data points n times for each iteration. One solution is to bin the data into a manageable number of points as was done in Ballard et al. (2010). We find that binning the data degrades the precision of our final solution. Binning the data results in average values for the measured flux and stellar centroid position that are not necessarily representative of the true variations in the stellar flux due to intrapixel sensitivity effects. We also find that the optimal σ_x and σ_y used in Equation B2 varies with the stellar centroid position. Ballard et al. (2010) used fixed values for σ_x and σ_y that empirically produces the lowest scatter. Using values for σ_x and σ_y that vary with centroid position gives us a lower scatter in the residuals compared to using fixed values for σ_x and σ_y .

Here we present an enhanced version of the Ballard et al. (2010) pixel mapping method that allows for a large number of data points and optimized values of σ_x and σ_y without being computationally prohibitive. In Equation B2, points that are outside $\sim 6\sigma_{x/y}$ of the position of the i th data point will contribute negligibly to the weighted

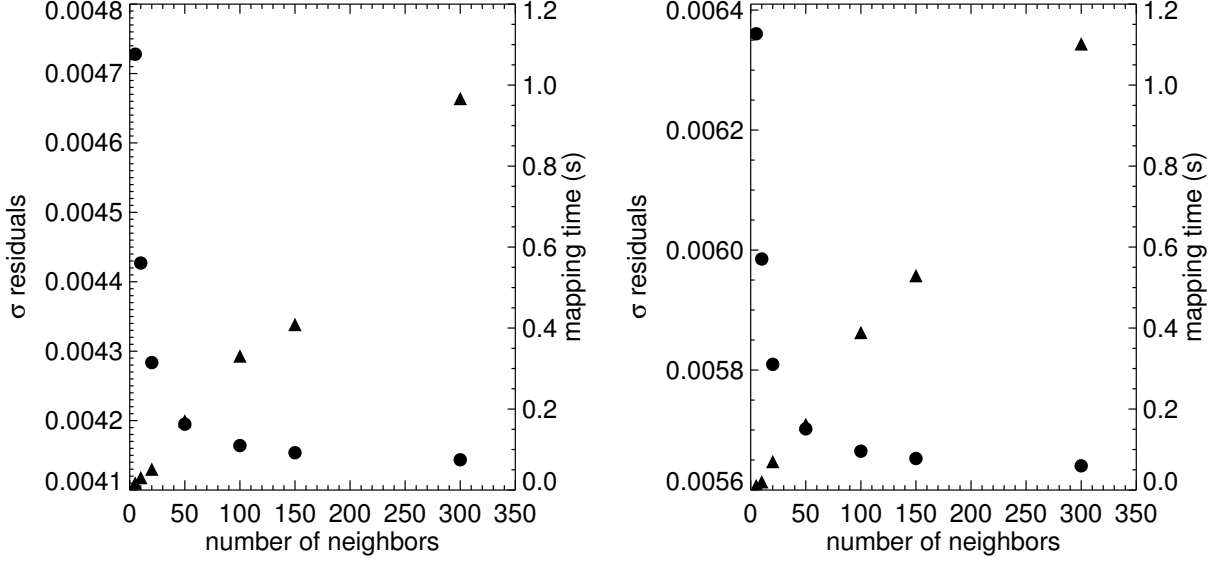


Figure 18. Standard deviation of the residuals (circles) and intrapixel sensitivity mapping time (triangles) as a function of the number of nearest neighbors included in the Gaussian weighting function (Equation B4) for the 3.6 μm (top) and 4.5 μm (bottom) observations. The standard deviation of the residuals from our fits decreases rapidly as the number of nearest neighbors considered is increased from 5 to 50 after which the gains in the precision of the fit are negligible. The time required to compute the full pixel map increases more or less linearly with the number of nearest neighbors. We find that repeated iterations become too computationally expensive when more than 50 nearest neighbors are considered. The computational time required per iteration is a multiple of the number of nearest neighbors and the 1.2 million data points in each of the 3.6 and 4.5 μm data sets.

sensitivity function $W(x_i, y_i)$. Given this fact, we reduce n in Equation B1 by only summing over a fixed number of nearest spatial neighbors. We determine the nearest neighbors to the i th flux measurement by the distance, r_i , given by

$$r_i = \sqrt{a(x_j - x_i)^2 + b(y_j - y_i)^2 + c(\tilde{\beta}_j^{1/2} - \tilde{\beta}_i^{1/2})^2} \quad (\text{B3})$$

where x_j , y_j , and $\tilde{\beta}_j$ are the position and noise pixel estimates for the j th image.

By including $\tilde{\beta}$ in Equation B3 we ensure that the nearest neighbors to the i th flux measurement share the same systematic effects. Although $\tilde{\beta}$ is not strictly a spatial parameter, as discussed in the Appendix variations in $\tilde{\beta}$ incorporate systematics that affect the shape of the PRF including and beyond intrapixel sensitivity variations. Our use of $\tilde{\beta}$ is similar to the incorporation of parameters for the PSF width and elongation in the correction of systematic variations as discussed in Bakos et al. (2010) for HATnet data. The factors a , b , and c in Equation B3 can be adjusted to give more weight to flux variations in a given spatial direction. For our 3.6 μm observations we find that the optimal value of $\sqrt{1/b}$ is 0.75 with $a = c = 1$. This difference in the a and b parameters accounts for the asymmetric shape of the IRAC PSF in the 3.6 μm bandpass (Gehrz et al. 2007). For our 4.5 μm observations we find that $a = b = c = 1$ is optimal although the results are similar if we assume $c = 0$.

We calculate the Gaussian smoothing kernel K for the i th data point with respect to its j th nearest neighbor, $K_i(j)$, according to

$$K_i(j) = \exp \left(- \frac{(x_j - x_i)^2}{2\sigma_{x,i}^2} - \frac{(y_j - y_i)^2}{2\sigma_{y,i}^2} - \frac{(\tilde{\beta}_j^{1/2} - \tilde{\beta}_i^{1/2})^2}{2\sigma_{\tilde{\beta}^{1/2},j}^2} \right), \quad (\text{B4})$$

where $\sigma_{x,i}$, $\sigma_{y,i}$, and $\sigma_{\tilde{\beta}^{1/2},i}$, are determined by the standard deviation of the x , y , and $\tilde{\beta}^{1/2}$ values for the n nearest neighbors. This formulation for $\sigma_{x,i}$, $\sigma_{y,i}$, and $\sigma_{\tilde{\beta}^{1/2},i}$ gives a wider filter in poorly sampled regions and narrower filter in regions with higher spatial resolution. Since the x , y , and $\tilde{\beta}$ vectors are independent of the fit parameters, we need only determine the n nearest neighbors and calculate $K_i(n)$ once for use in our iterative fitting routines.

When selecting the optimal number of nearest neighbors to use in this calculation, there is a direct tradeoff between increased precision and increased computational time. Figure 18 shows the change in the standard deviation of the residuals and the time required to compute $F_{0,j}$ for all j as a function of the number of nearest neighbors used. We find that using more than 50 nearest neighbors reduces the standard deviation of the residuals by less than 1%. We also

find a significant increase in the computational time required to use more than 20-50 nearest neighbors. We therefore elect to limit the number of nearest neighbors considered in our calculation of Equation B4 to 50.

REFERENCES

- Agol, E., Cowan, N. B., Knutson, H. A., et al. 2010, *ApJ*, 721, 1861
 Albrecht, S., Winn, J. N., Johnson, J. A., et al. 2012, *ApJ*, 757, 18
 Bakos, G., Noyes, R. W., Kovács, G., et al. 2004, *PASP*, 116, 266
 Bakos, G. Á., Lázár, J., Papp, I., Sári, P., & Green, E. M. 2002, *PASP*, 114, 974
 Bakos, G. Á., Shporer, A., Pál, A., et al. 2007a, *ApJ*, 671, L173
 Bakos, G. Á., Kovács, G., Torres, G., et al. 2007b, *ApJ*, 670, 826
 Bakos, G. Á., Torres, G., Pál, A., et al. 2010, *ApJ*, 710, 1724
 Ballard, S., Charbonneau, D., Deming, D., et al. 2010, *PASP*, 122, 1341
 Baraffe, I., Chabrier, G., & Barman, T. 2008, *A&A*, 482, 315
 Barnes, J. W., & O'Brien, D. P. 2002, *ApJ*, 575, 1087
 Batygin, K., Bodenheimer, P., & Laughlin, G. 2009, *ApJ*, 704, L49
 Bean, J. L., Benedict, G. F., Charbonneau, D., et al. 2008, *A&A*, 486, 1039
 Beerer, I. M., Knutson, H. A., Burrows, A., et al. 2011, *ApJ*, 727, 23
 Bodenheimer, P., Lin, D. N. C., & Mardling, R. A. 2001, *ApJ*, 548, 466
 Burrows, A., Budaj, J., & Hubeny, I. 2008, *ApJ*, 678, 1436
 Carter, J. A., & Winn, J. N. 2009, *ApJ*, 704, 51
 Charbonneau, D., Knutson, H. A., Barman, T., et al. 2008, *ApJ*, 686, 1341
 Charbonneau, D., Allen, L. E., Megeath, S. T., et al. 2005, *ApJ*, 626, 523
 Cowan, N. B., & Agol, E. 2008, *ApJ*, 678, L129
 —. 2011, *ApJ*, 726, 82
 Cowan, N. B., Machalek, P., Croll, B., et al. 2012a, *ApJ*, 747, 82
 Cowan, N. B., Voigt, A., & Abbot, D. S. 2012b, *ApJ*, 757, 80
 Demory, B.-O., Seager, S., Madhusudhan, N., et al. 2011, *ApJ*, 735, L12
 Eastman, J., Siverd, R., & Gaudi, B. S. 2010, *PASP*, 122, 935
 Eggleton, P. P., Kiseleva, L. G., & Hut, P. 1998, *ApJ*, 499, 853
 Fabrycky, D. 2008, *ApJ*, 677, L117
 Fabrycky, D., & Tremaine, S. 2007, *ApJ*, 669, 1298
 Fazio, G. G., Hora, J. L., Allen, L. E., et al. 2004, *ApJS*, 154, 10
 Ford, E. B. 2005, *AJ*, 129, 1706
 Fortney, J. J., Marley, M. S., & Barnes, J. W. 2007, *ApJ*, 659, 1661
 Gehrz, R. D., Roellig, T. L., Werner, M. W., et al. 2007, *Review of Scientific Instruments*, 78, 011302
 Harris, W. E. 1990, *PASP*, 102, 949
 Hauschildt, P. H., Allard, F., & Baron, E. 1999, *ApJ*, 512, 377
 Holman, M. J., & Murray, N. W. 2005, *Science*, 307, 1288
 Hut, P. 1981, *A&A*, 99, 126
 Iro, N., & Deming, L. D. 2010, *ApJ*, 712, 218
 Ivanov, P. B., & Papaloizou, J. C. B. 2007, *MNRAS*, 376, 682
 Jackson, B., Greenberg, R., & Barnes, R. 2008, *ApJ*, 678, 1396
 Jenkins, J. M., Caldwell, D. A., & Borucki, W. J. 2002, *ApJ*, 564, 495
 Kane, S. R., & Gelino, D. M. 2010, *ApJ*, 724, 818
 Kataria, T., Showman, A. P., Lewis, N. K., et al. 2012, *ArXiv e-prints*
 Kipping, D. M. 2009, *MNRAS*, 392, 181
 Kipping, D. M., & Spiegel, D. S. 2011, *MNRAS*, 417, L88
 Knutson, H. A., Charbonneau, D., Allen, L. E., Burrows, A., & Megeath, S. T. 2008, *ApJ*, 673, 526
 Knutson, H. A., Charbonneau, D., Cowan, N. B., et al. 2009a, *ApJ*, 703, 769
 Knutson, H. A., Howard, A. W., & Isaacson, H. 2010, *ApJ*, 720, 1569
 Knutson, H. A., Charbonneau, D., Allen, L. E., et al. 2007, *Nature*, 447, 183
 Knutson, H. A., Charbonneau, D., Cowan, N. B., et al. 2009b, *ApJ*, 690, 822
 Knutson, H. A., Lewis, N., Fortney, J. J., et al. 2012, *ApJ*, 754, 22
 Kozai, Y. 1962, *AJ*, 67, 591
 Langton, J., & Laughlin, G. 2008, *ApJ*, 674, 1106
 Lewis, N. K., Showman, A. P., Fortney, J. J., et al. 2010, *ApJ*, 720, 344
 Liddle, A. R. 2007, *MNRAS*, 377, L74
 Lin, D. N. C., Bodenheimer, P., & Richardson, D. C. 1996, *Nature*, 380, 606
 Loeillet, B., Shporer, A., Bouchy, F., et al. 2008, *A&A*, 481, 529
 Mandel, K., & Agol, E. 2002, *ApJ*, 580, L171
 Markwardt, C. B. 2009, in *Astronomical Society of the Pacific Conference Series*, Vol. 411, *Astronomical Data Analysis Software and Systems XVIII*, ed. D. A. Bohlender, D. Durand, & P. Dowler, 251
 Matsumura, S., Takeda, G., & Rasio, F. A. 2008, *ApJ*, 686, L29
 Mighell, K. J. 2005, *MNRAS*, 361, 861
 Morales-Calderón, M., Stauffer, J. R., Kirkpatrick, J. D., et al. 2006, *ApJ*, 653, 1454
 Muller, R. A., & Buffington, A. 1974, *Journal of the Optical Society of America (1917-1983)*, 64, 1200
 Murray, C. D., & Dermott, S. F. 1999, *Solar system dynamics*, ed. Murray, C. D. & Dermott, S. F.
 Naoz, S., Farr, W. M., Lithwick, Y., Rasio, F. A., & Teysseandier, J. 2011, *ArXiv e-prints*
 Pál, A. 2008, *MNRAS*, 390, 281
 Pál, A., Bakos, G. Á., Torres, G., et al. 2010, *MNRAS*, 401, 2665
 Pritchett, C., & Kline, M. I. 1981, *AJ*, 86, 1859
 Rasio, F. A., & Ford, E. B. 1996, *Science*, 274, 954
 Reach, W. T., Megeath, S. T., Cohen, M., et al. 2005, *PASP*, 117, 978
 Sasaki, T., Barnes, J. W., & O'Brien, D. P. 2012, *ApJ*, 754, 51

- Showman, A. P., Cho, J. Y.-K., & Menou, K. 2010, *Atmospheric Circulation of Exoplanets*, ed. Seager, S., 471–516
- Showman, A. P., Fortney, J. J., Lian, Y., et al. 2009, *ApJ*, 699, 564
- Showman, A. P., & Guillot, T. 2002, *A&A*, 385, 166
- Sing, D. K. 2010, *A&A*, 510, A21
- Southworth, J. 2008, *MNRAS*, 386, 1644
- Stevenson, K. B., Harrington, J., Nymeyer, S., et al. 2010, *Nature*, 464, 1161
- Stevenson, K. B., Harrington, J., Fortney, J., et al. 2011, *ArXiv e-prints*
- Todorov, K. O., Deming, D., Knutson, H. A., et al. 2012, *ApJ*, 746, 111
- Vogt, S. S., Allen, S. L., Bigelow, B. C., et al. 1994, in *Society of Photo-Optical Instrumentation Engineers (SPIE) Conference Series*, Vol. 2198, *Society of Photo-Optical Instrumentation Engineers (SPIE) Conference Series*, ed. D. L. Crawford & E. R. Craine, 362
- Weidenschilling, S. J., & Marzari, F. 1996, *Nature*, 384, 619
- Werner, M. W., Roellig, T. L., Low, F. J., et al. 2004, *ApJS*, 154, 1
- Winn, J. N. 2010, *Exoplanet Transits and Occultations*, ed. S. Seager, 55–77
- Winn, J. N., Johnson, J. A., Albrecht, S., et al. 2009, *ApJ*, 703, L99
- Winn, J. N., Johnson, J. A., Peek, K. M. G., et al. 2007a, *ApJ*, 665, L167
- Winn, J. N., Holman, M. J., Bakos, G. Á., et al. 2007b, *AJ*, 134, 1707
- Winn, J. N., Holman, M. J., Torres, G., et al. 2008, *ApJ*, 683, 1076
- Wizinowich, P., Acton, D. S., Shelton, C., et al. 2000, *PASP*, 112, 315
- Wu, Y., & Lithwick, Y. 2011, *ApJ*, 735, 109
- Wu, Y., & Murray, N. 2003, *ApJ*, 589, 605